

Aggregation-Induced Emission-Active Hydrazone-Based Probe: Selective Sensing of Al^{3+} , HF_2^- , and Nitro Explosives

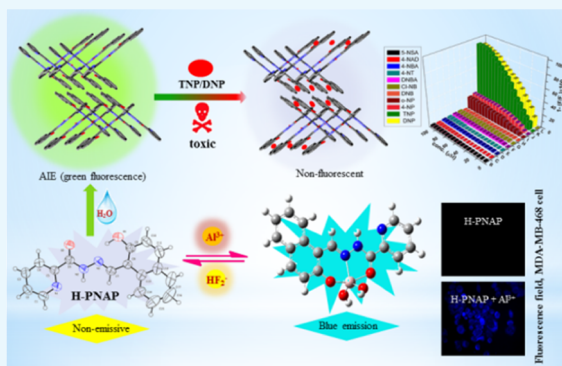
Sunanda Dey,[†] Rakesh Purkait,[†] Kunal Pal,^{‡,§} Kuladip Jana,[§] and Chittaranjan Sinha^{*,†,§}

[†]Department of Chemistry and [‡]Department of Life Science and Biotechnology, Jadavpur University, Kolkata 700032, India

[§]Division of Molecular Medicine and Centre for Translational Research, Bose Institute, Kolkata 700056, India

Supporting Information

ABSTRACT: (*E*)-*N'*-((2-Hydroxynaphthalen-1-yl)methylene)-picolinohydrazide (H-PNAP) shows aggregation-induced emission (AIE) strictly in a 90% water/MeOH (v/v) mixture at 540 nm, and the solid-state emission is blue-shifted to 509 nm upon excitation at 400 nm. The AIE activity of H-PNAP is selectively quenched by 2,4,6-trinitrophenol (TNP) and 2,4-dinitrophenol (DNP) out of different nitroaromatic compounds with a limit of detection (LOD) of 7.79×10^{-7} and 9.08×10^{-7} M, respectively. The probe is nonemissive in aqueous medium (4-(2-hydroxyethyl)-1-piperazineethanesulfonic acid, HEPES buffer, pH 7.2); however, it shows a strong emission to Al^{3+} (λ_{em} 490 nm) in the presence of 17 other biological metal ions, and the LOD is 2.09 nM which is far below the WHO recommended value (7.41 mM). The emission of the $[\text{Al}(\text{PNAP})-(\text{NO}_3)_2]$ complex is quenched by HF_2^- (F^- and PO_4^{3-} are weak quencher), and the LOD is as low as 15 nM. The probable mechanism of the sensing feature of the probe has been authenticated by ^1H nuclear magnetic resonance titration, mass spectrometry, Fourier transform infrared spectroscopy, Benesi–Hildebrand plot, and Job's plot in each case. The probe has some practical applications such as recovery of Al^{3+} from the drinking water sample, construction of the INHIBIT logic gate, and detection kits for Al^{3+} and TNP/DNP by simple paper test strips. The probe, H-PNAP, has successfully been applied to the detection of intracellular Al^{3+} and HF_2^- ions in the human breast cancer cell, MDA-MB-468.



INTRODUCTION

Heavier cations (higher than Zn^{2+}) are commonly toxic and some lower atomic weight cations like Be^{2+} and Al^{3+} are not welcome by human cells.¹ Besides, the concentration of ions has imperative impact to regulate the biochemical activity and the rates of the reactions in living cells. Even essential ions in higher or lower concentration than that of biological concentration are fatal to human health.² Therefore, accurate and precise measurement of ions at a very low concentration level is important in chemistry and biology. One of the important metals, aluminum (Al), has huge applications in the society because of noncorrosive nature, good conductivity, use in making cooking utensils, potable water supplies, cosmetics, and so forth.^{3,4} Thus, Al enters into human body easily and may be responsible for neurotoxicity, bone deformation, disruption of reproduction, and so forth.⁵ This is one of the reasons for the detection of Al^{3+} in drinking water, food, beverages, and so forth. Al(III), a p-block element, does not form colored complexes, and its measurement needs special design of chemosensors.

In recent times, the design of sensors (ions or small molecules) and their application in live cells for the detection of ions/molecules have received active interest from chemistry, physics, chemical engineering, electrical and electronic

engineering, and many other branches. On considering the social and biological importance of Al(III), some examples of fluorescent sensors have been reported for Al^{3+} detection with the Schiff base scaffold of 4-aminoantipyrine derivatives,⁶ rhodamine B ligands,⁷ coumarinyl derivatives,⁸ benzophenone,⁹ chromone,¹⁰ diphenyl pyrrol derivatives,¹¹ pyrazoles,¹² quinolones,¹³ fluorenes,¹⁴ benzimidazoles,¹⁵ and so forth. Besides, a limited number of sensors exhibit aggregation-induced emission (AIE), and their emissivity, in some cases, has been influenced by Al^{3+} ions.¹⁶ Literature review shows that functionalized naphthyl, polyaromatic hydrocarbon (PAH) scaffolds, phenolphthalein-based probe, metal–organic-frameworks (MOFs),¹⁷ and so forth are specifically important for ion-sensing research. Hydrazone function has been commonly used in the detection of ions.¹⁸ Furthermore, picolinohydrazide attached with naphthyl scaffold is a well-known fluorophore for its selective and sensitive ion-sensing activity.¹⁹ In this work, we have designed hitherto an unknown probe (*E*)-*N'*-((2-hydroxynaphthalen-1-yl)methylene)-picolinohydrazide (H-PNAP), which serves as highly sensitive

Received: February 8, 2019

Accepted: April 30, 2019

Published: May 14, 2019

for the detection of Al(III) at nM concentration (limit of detection, LOD, 2.09 nM).

Anions are also useful to maintain fluid ionic pressure, nerve impulse, ion transportation, and so forth; however, some of the anions are toxic to human health and aquatic environment, such as HF_2^- , CN^- , AsO_4^{3-} , AsO_3^{3-} (AsO_2^-), F^- , NO_3^- , NO_2^- , and so forth. Over the last two decades, several efforts have been devoted to design several receptors for anionic species.²⁰ There are two approaches to design anion sensors—N-heterocyclic fluorogenic species which on protonation may enhance emission which could capable to form hydrogen bond with anions and binding strength may regulate emission efficiency; and/or emissive metal complexes may chemically prefer specific anion to eject M^{n+} from the sensor cavity and emission intensity is quenched or wavelength is shifted. These signaling processes have been used for quantitative identification of anions. Herein, the emissive Al^{3+} –H-PNAP complex serves as a sensitive fluorogenic detector of HF_2^- .

The probe, H-PNAP, undergoes aggregation and shows AIE. The AIE property of naphthyl–picolinyl hydrazide (H-PNAP) shows an amazing sensitivity to detect nitro-explosives, mainly 2,4,6-trinitrophenol (TNP) and 2,4-dinitrophenol (DNP). The nitro-explosives are used in terroristic activities and become a concern to the Crime Bureau of Intelligence and Home Department of the government.^{21–23} Although many other methods of detection of nitro-explosives such as, police dog detection, plasma desorption mass spectrometry, ion migration spectrum, energy-dispersive X-ray diffraction, surface-enhanced Raman spectroscopy, or additional imaging techniques are known,^{24–29} none of them are economically viable. However, fluorescence-based explosive detection is commercially realistic, of high-speed, and portable.³⁰ Thus, the probe, H-PNAP, is useful for Al^{3+} , HF_2^- , and nitrophenol detection. The probe, H-PNAP, is characterized by single-crystal X-ray diffraction measurement along with other spectroscopic data.

RESULTS AND DISCUSSION

Synthesis and Formulation of the Probe. The condensation of picolinohydrazide and 2-hydroxy-1-naphthaldehyde in dry MeOH has synthesized the probe H-PNAP (Scheme S1), and the ^1H nuclear magnetic resonance (NMR) spectrum (dimethylsulfoxide, $\text{DMSO}-d_6$) shows the characteristic peaks at 12.73 (s, 1H, OH), 12.38 (s, 1H, NH), and 9.62 (s, 1H, imine-H) which supports the structure of the probe (Figure S1). The ^{13}C NMR (in $\text{DMSO}-d_6$) spectrum also supports the presence of signals at 160.49 ($\text{C}=\text{O}$), 158.63 ($\text{C}=\text{N}$), and others (Figure S2). Electrospray ionization mass spectrometry (ESI-MS) spectrum also shows the ion peak at 292.1084 which resembles the formation of $[\text{H-PNAP} + \text{H}]^+$ and at 314.0985 for $[\text{H-PNAP} + \text{Na}]^+$ (base peak) (Figure S3). The IR spectrum shows $\nu(\text{C}=\text{N})$ at 1620 cm^{-1} , $\nu(\text{C}=\text{O})$ at 1661 cm^{-1} , $\nu(\text{NH})$ at 3191 cm^{-1} , and $\nu(\text{phenolic-OH})$ at 3482 cm^{-1} (Figure S4). The yellow X-ray diffractable crystal of H-PNAP belongs to the monoclinic system of space group $P2_1/n$ (Figure 1). The reaction of the methanol solution of $\text{Al}(\text{NO}_3)_3$ with H-PNAP separates the orange-colored $[\text{Al}(\text{PNAP})(\text{NO}_3)_2]$ which shows the characteristic ^1H NMR (δ , ppm) (500 MHz, $\text{DMSO}-d_6$) singlet peak at 12.388 ppm for $-\text{NH}$ and $\text{CH}=\text{N}$ at 9.624 ppm along with other peaks (Figure S5); the ESI-MS peak for the $\text{HPNAP}-\text{Al}^{3+}$ complex appears at 442.1086 (calculated mass of $[\text{Al}(\text{PNAP})(\text{NO}_3)_2]$, 442.06) (Figure S6) and the IR spectrum (Figure S7) shows $\nu(\text{NH})$,

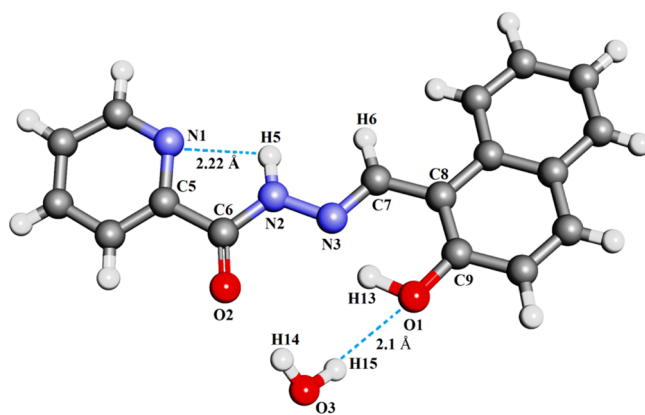


Figure 1. Molecular structure of the probe, H-PNAP.

3110 ; $\nu(\text{C}=\text{O})$, 1662 ; $\nu(\text{C}=\text{N})$, 1612 cm^{-1} ; and $\nu(\text{NO}_3)$, 1388 cm^{-1} .

The picolinoyl hydrazide and naphthyl moieties are linked by an imine ($\text{C}=\text{N}$) bond. An intramolecular hydrogen bond is present between N(1) and H(5) with a bond distance of 2.22 Å and an intermolecular H bond is also present between O(1) and H(15) with a bond distance of 2.1 Å (Figure 1). The details about the crystal structure, important distance, and bond angles are incorporated in Tables S1 and S2 in the Supporting Information. In a single unit, there is a water molecule, and this water molecule can form layer-to-layer intermolecular H-bonding interactions (Figure 2a). Wave-like supramolecular aggregation is formed by weak $\pi\cdots\pi$ interactions of the probe (Figure 2b).

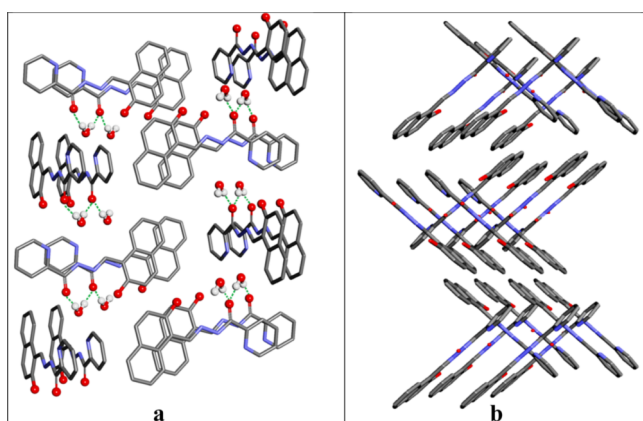


Figure 2. (a) Layer-to-layer H-bonding interactions with water molecules and (b) wave-like supramolecular aggregation of the probe.

Photophysics and Application of AIE Property. The UV–vis spectrum of H-PNAP in methanol shows absorption bands at 326 and 366 nm, which are assigned to $\pi_{\text{naphthyl}} \rightarrow \pi_{\text{picolinohydrazide}}$ transitions that have been supported by the time-dependent density functional theory (TDDFT)/conductor-like polarizable continuum model (CPCM) method of computation. In solid state, these bands are red-shifted by 25–40 nm. The excitation of the probe in crystal state at 400 nm exhibits high-intense green fluorescence (λ_{em} , 509 nm) (Figure 3). The fluorescence spectrum of the probe, H-PNAP, in amorphous phase is also recorded (Figure S8), and it exhibits a strong emission, but weaker than the emission in the crystalline state. The rapport of these observations is that the compound has

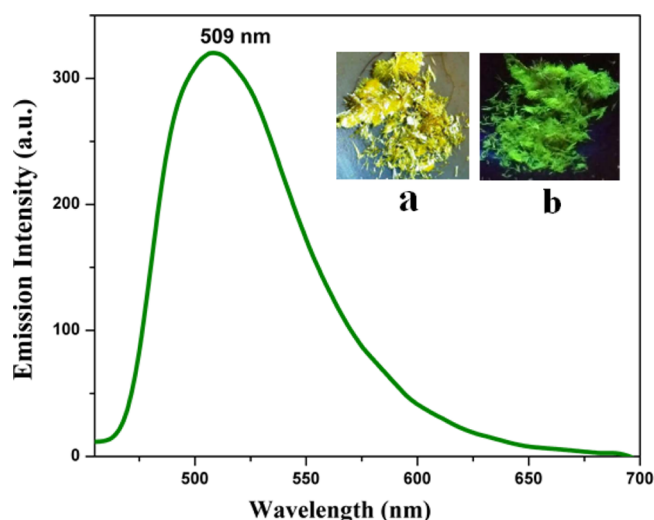
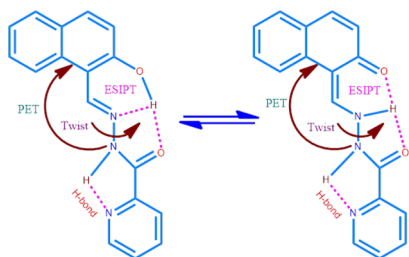


Figure 3. Solid-state fluorescence spectrum of H-PNAP on excitation by 400 nm; inset: images of H-PNAP crystals (a) under normal light and (b) under UV (λ , 365 nm) light.

crystallization-induced emission enhancement property.³¹ Restriction of different physical processes like rotation, vibration, and isomerization in the solid state helps the emission process, whereas the solution phase of H-PNAP in pure MeOH and pure aqueous medium is nonemissive. In a pure solvent solution, the excited-state proton transfer (ESIPT), twisting, and photoinduced electron transfer (PET) processes (Scheme 1) may be active to inhibit the energy emission program.

Scheme 1. Deactivation Processes of Excited H-PNAP by PET, Twisting, and ESIPT



Although the pure methanol solution of H-PNAP is nonemissive, addition of water to this solution shows an amazing experience and becomes strongly emissive in a 90% binary mixture of H₂O–MeOH (v/v) solution (Figure 4). From 0 to 83% water/MeOH binary mixture of the probe, no emission is perceived, and AIE starts at 84% water/MeOH mixture and increases gradually up to 90% water content (Figures 4a and S9). Figure 4a shows that with an increase in the percentage of water in MeOH (from 84 to 90% water/MeOH), the emission band is shifted bathochromically (509–540 nm). This red shift in emission maxima arises because of J-type aggregation by the packing between monomers. Kasha's exciton theory announced that the J aggregation of an analyte should red shift the emission band compared to monomer emission; this is because of transition to a lower excitonic state.³² This AIE is maximum at 90% water content, and after this the emission intensity decreases, which indicates that on further addition of water (>90%) the aggregates may be

ruptured that causes a decrease in emission intensity. This indicates that the probe (H-PNAP) is AIE-active. PAHs such as naphthalene, anthracene, acridine, pyrene, and so forth aggregate in solution upon changing the polarity of the solution and generally quench the emission process.¹⁶ Tang et al., in 2001, reported a contradictory observation where aggregation assisted the enhancement of emission.³³ For the biosensing and imaging applications, the AIE-active fluorogenic probes have been exploited to function as novel optical materials.¹⁶ The AIE effect may be because of the high rigidity of the probe in aggregated state which may cause restriction of intramolecular rotation.^{34–36} The change of the absorption spectral feature is also distinctive upon dilution of the MeOH solution of H-PNAP with water (Figure 4b). Not only emission spectra but absorption spectra (Figure 4b) also show red-shifting upon change in the percentage of water content to the MeOH solution. In a pure MeOH solution of H-PNAP, the absorbance bands appear at 326 and 366 nm, and upon addition of water to this solution, a new band appears at 401 nm, which is also an indication of J-aggregates.³⁷

The aggregation has been supported by dynamic light scattering (DLS) and field emission scanning electron microscopy (FESEM) data (vide infra). Some morphological and structural changes are obtained by FESEM (Figure 5) with the dilution of the probe H-PNAP from 0 to 90% water in MeOH. The probe in the pure methanol solution is a fibrous-shaped nanomaterial (26 ± 2.1 nm), whereas in the aggregated phase (90% water content), it has slipped bark (130 ± 7.4 nm)-like geometry. Again, changes in particle size are observed on changing the percentage of water content, that is, from 0 to 100% (v/v) MeOH–water by DLS measurements. For 0, 30, 90, and 100% water content in the binary mixture of the probe, the average diameters of the probe increase and are 30, 178, 391 and 305 nm, respectively (Figure S10). At 90% water content, the average diameter is maximum; this may be because of the reason of the highest number of excimers aggregated, and on increasing the dilution to 90–100% by water, there is a decrease in particle size, which can be because of the hydrolysis of the aggregates via the solvation process.

The emission of the aggregated phase is supported by optical fluorescence microscopic images (Figure 6). In pure methanol, H-PNAP does not show any emission with UV light excitation, but in the presence of 90% water content in MeOH, the probe, H-PNAP, shows a strong green emission. The fluorescence properties in the aggregated state are recognized for the fabrication of organic light-emitting diode material.³⁸

Lifetime (τ) and quantum yield (ϕ) information also support longer stability and the highest ϕ of H-PNAP in the 90% water/MeOH mixture (τ , 1.01 ns; ϕ , 0.496) than pure water (τ , 0.98 ns; ϕ , 0.253), pure MeOH (τ , 0.0547 ns; ϕ , 0.0023), and 30% water/MeOH medium (τ , 0.113 ns; ϕ , 0.018) (Figure S11 and Table S3). The quantum yield of H-PNAP is 215 times increased, from 0.0023 to 0.496, by changing the percentage of water content in the binary mixture (H₂O/MeOH) from 0 to 90%. From this observation, we found that with an increase in the percentage of water, the quantum yield (ϕ) of H-PNAP increases up to 90% water content, and then at 100% water content it decreases, which are supportive with the photophysical properties of the reported J-type aggregation.^{39,40}

Nitroaromatics Sensing. The reversibility of the highly emissive aggregated probe, H-PNAP (90% water/MeOH), is

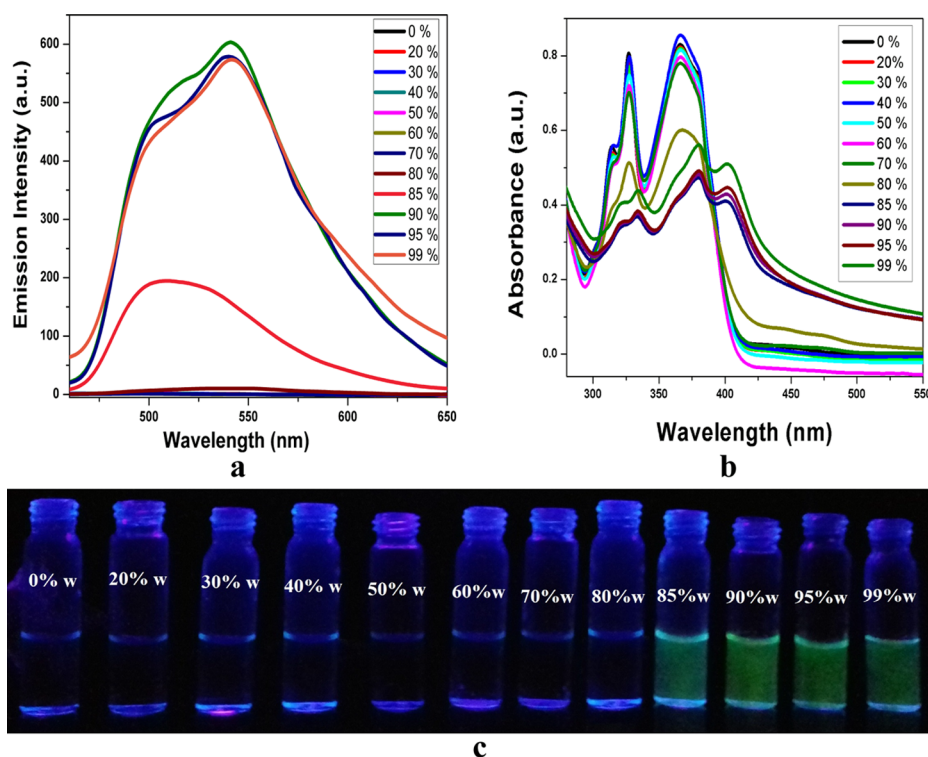


Figure 4. Spectral change of H-PNAP ($50 \mu\text{M}$) with an increase in the percentage of water in MeOH; (a) fluorescence (λ_{exc} 400 nm), (b) absorbance, and (c) image of AIE of H-PNAP under UV irradiation (λ , 365 nm).

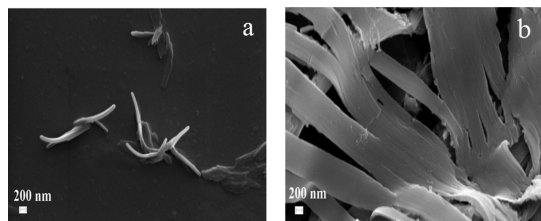


Figure 5. FESEM images: (a) H-PNAP in pure MeOH (26 ± 2.1 nm) and (b) H-PNAP in 90% water/MeOH (v/v) (130 ± 7.4 nm). (Scale bar = 200 nm).

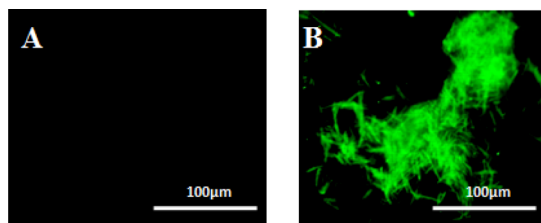
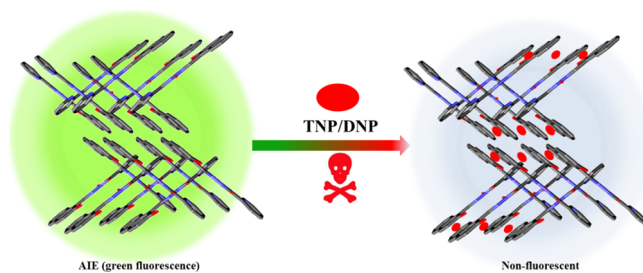


Figure 6. Optical fluorescence microscopic images (solid state) of (A) H-PNAP ($50 \mu\text{M}$) in MeOH and (B) H-PNAP ($50 \mu\text{M}$) in 90% water/MeOH with UV light excitation.

tested by various nitroaromatic compounds (NACs) like 4-nitrophenol (4-NP), TNP, DNP, 4-chloronitrobenzene (Cl-NB), 1,3-dinitrobenzene (DNB), *O*-nitrophenol (*O*-NP), 3,5-dinitrobenzoic acid, 4-nitrotoluene, 4-nitrobenzoic acid, 4-nitroacetanilide, and 5-nitro salicylic acid. High-intensity fluorescence emission at 540 nm for the aggregated H-PNAP (90% water/MeOH) is selectively quenched in the presence of TNP and DNP only, out of the 11 NACs (Figure S12), and this may be because of the interaction of NACs (TNP and DNP) with the aggregated probe and can hamper the

aggregation phenomena (Scheme 2). NACs are electron-deficient, and the probe H-PNAP is electron-rich; hence,

Scheme 2. Insertion of TNP/DNP to the Aggregated Probe H-PNAP



electron transfer may initiate from the excited H-PNAP to the analyte (TNP/DNP) and hence quenching. The quenching of fluorescence of the aggregated probe by NAC explosives may arise through the PET mechanism (Scheme S2).⁴¹ The quenching efficiency (%) of the aggregated fluorescence (λ_{em} , 540 nm; v/v, 9:1 $\text{H}_2\text{O}/\text{MeOH}$) of H-PNAP ($50 \mu\text{M}$) upon addition of different NACs with different concentrations is also checked, and it shows that among all the NACs, only TNP and DNP show the highest quenching efficiency around 95 and 92%, respectively (Figure 7).

Upon gradual addition of the TNP/DNP solution ($0.01 \text{ mL} \times 10^{-3} \text{ M}$) to aggregated H-PNAP (90% water/MeOH), the emission intensity gradually decreases (Figure S13). The detection limits (3σ method) are $0.779 \mu\text{M}$ (TNP) and $0.908 \mu\text{M}$ (DNP) (Figures S14 and S15) and the quenching constants are $2.1 \times 10^4 \text{ M}^{-1}$ (TNP) and $3.2 \times 10^4 \text{ M}^{-1}$ (DNP) (Figures S16 and S17). There are some reports of MOFs,⁴² metal complexes,⁴³ and simple molecules^{35,44–46} that

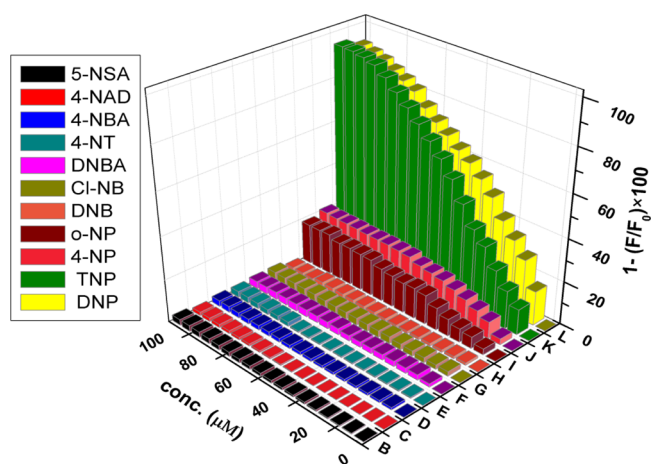


Figure 7. Quenching efficiency (%) of the excimer fluorescence of H-PNAP (50 μM) in 9:1 $\text{H}_2\text{O}/\text{MeOH}$ upon addition of different NACs at λ_{em} , 540 nm with λ_{ex} , 400 nm.

serve as chemosensors for the detection of TNP and DNP within the detection range 0.23–2.25 μM (Table S4), and the present result also appears in this detection range. H-PNAP in 90% water/MeOH solution is emissive in the wide pH range (2–12), and TNP/DNP can quench this emission in this varied pH range also (Figure S18).

The UV–vis absorption spectral change of H-PNAP (50 μM) in the AIE phase (90% water content) in the presence of TNP/DNP (2 equiv) (Figure S19) may also be explained on considering the formation of charge-transfer complex by the strong interaction of the electron-deficient TNP/DNP and π electron-rich naphthyl fluorophore.^{47,48}

The fluorescence intensity ratio (F_0/F) has been plotted against the concentration of TNP and DNP, and the nonlinear Stern–Volmer plots (Figure 8) are obtained which may be because of static and dynamic quenching. To understand the insight mechanism, the fluorescence lifetime measurement of the sensor in the presence and absence of the quencher is carried out. The static quenching appears because of the binding of the sensor with the quencher at the ground state, and the dynamic quenching exists by diffusion-controlled collisions between the excited sensor and the quencher.³⁵ The fluorescence lifetime decay of H-PNAP (90% water/MeOH) remains intact both for TNP and DNP with different concentrations (5–100 μM) (Figures S20 and S21, Table S5), which demonstrates that the fluorescence quenching of

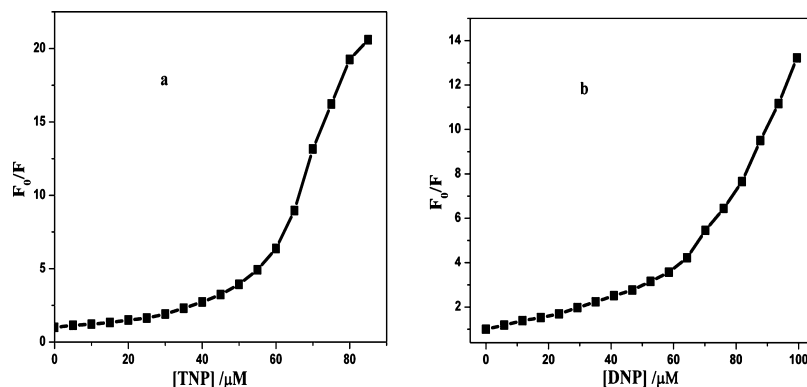


Figure 8. Plot of F_0/F against the concentration of (a) TNP and (b) DNP.

the aggregated state occurs through a static mechanism by TNP and DNP, and an upward deviation may arise because of the incredible quenching ability at higher concentrations of TNP and DNP.

Ion-Sensing Activity of the Probe. In a pure aqueous medium (4-(2-hydroxyethyl)-1-piperazineethanesulfonic acid—HEPES buffer, pH 7.2), the probe H-PNAP does not show any emission behavior upon excitation at 400 nm. Addition of biologically active cations viz., Na^+ , K^+ , Ca^{2+} , Mg^{2+} , Mn^{2+} , Fe^{2+} , Zn^{2+} , Cd^{2+} , Cr^{3+} , Co^{2+} , Ni^{2+} , Pd^{2+} , Hg^{2+} , Cu^{2+} , Ba^{2+} , and Pb^{2+} in the aqueous solution of H-PNAP again has no significant change in the emission pattern and intensity. Upon addition of Al^{3+} in the pure aqueous medium (HEPES buffer, pH 7.2) of H-PNAP, the emission is increased nearly by 500-fold at 490 nm (Figure 9). In pure water solution, the

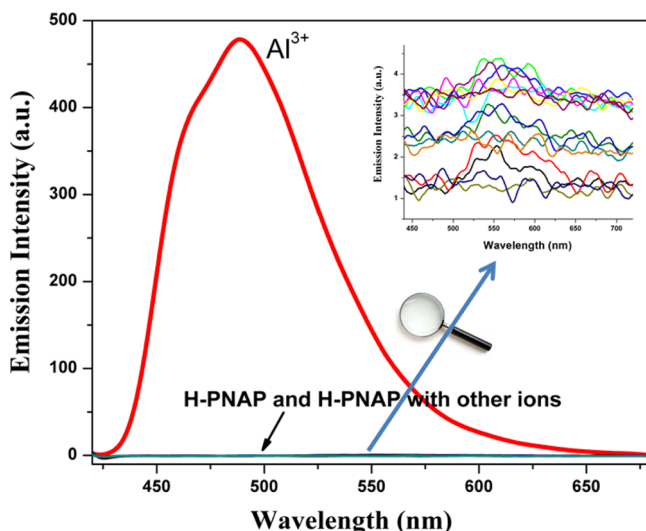


Figure 9. Change in the emission spectrum of H-PNAP (50 μM) upon gradual addition of different metal ions (50 μM each) in pure water (HEPES buffer, pH 7.2); λ_{ex} , 400 nm; inset: zooming image for H-PNAP and H-PNAP with other metal ions.

absorption peaks at 326, 366, and 440 nm of H-PNAP are observed. With an incremental addition of Al^{3+} in the pure aqueous medium (HEPES buffer, pH 7.2), the probe shows a gradual decrease in the intensity of absorption bands at 326 and 366 nm with the generation of a new band at 406 nm, forming an isosbestic point at 388 nm (Figure S22). This observation may be because of the existence of intramolecular

charge-transfer transition through chelation.⁴⁹ The absorbance spectra are unchanged until the stoichiometry satisfies 1:1 molar ratio between H-PNAP and Al^{3+} and no longer changes with further addition of Al^{3+} in the solution of the probe.

Naphthalene is a considerably potential fluorogenic agent, but the probe H-PNAP is nonemissive in a pure MeOH or a pure aqueous medium. The probe may form an intramolecular hydrogen bond and ESIPT which may be the reasons for nonradiative energy transfer of the excited state along with PET, twisting the process of quenching. Upon the addition of Al^{3+} out of a large number of biologically active cations viz. Na^+ , K^+ , Ca^{2+} , Mg^{2+} , Mn^{2+} , Fe^{2+} , Zn^{2+} , Cd^{2+} , Cr^{3+} , Co^{2+} , Ni^{2+} , Pd^{2+} , Hg^{2+} , Cu^{2+} , Ba^{2+} , and Pb^{2+} , the enhancement of emission may be explained by restricting ESIPT, PET, twisting, and inclusion of CHEF (Scheme S3).⁵⁰ The interaction of H-PNAP with Al^{3+} is also investigated by fluorimetric titration (Figure 10), and the LOD for Al^{3+} is 2.09 nM (3σ method,

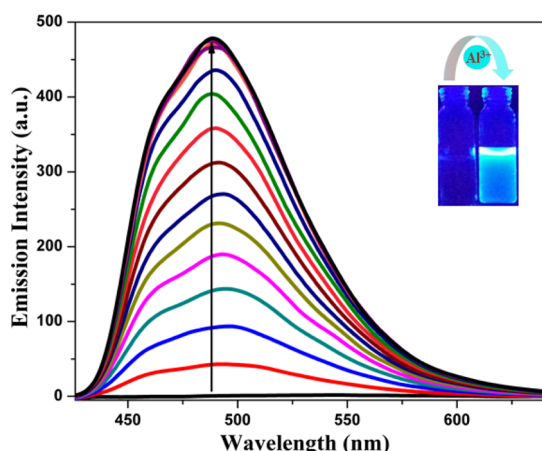


Figure 10. Change in emission spectra of H-PNAP (50 μM) upon gradual addition of Al^{3+} ions (0–50 μM) in pure water (HEPES buffer, pH 7.2) (λ_{ex} , 400 nm); inset: emission under UV light (λ , 365 nm) for H-PNAP in the absence and presence of Al^{3+} (50 μM).

Figure S23). Benesi–Hildebrand equation, $[(F_{\text{max}} - F_0)/(F - F_0)]$ versus $1/[\text{Al}^{3+}]$, has been used (Figure S24) to calculate the binding constant, K_d ($4.6 \times 10^4 \text{ M}^{-1}$). Use of naphthyl-appended fluorogenic scaffold for identification of very small quantity of Al^{3+} ions is known in the literature^{51–54} (Table S6), and the present work reports the lowest LOD among them.

The stability of the excited probe and its aluminum complex, $[\text{Al}(\text{PNAP})(\text{NO}_3)_2]$, has been checked by fluorescence lifetime measurements. Both the probe and its complex show biexponential fluorescence decay profile with average lifetimes of 1.00 and 1.73 ns, respectively (Figure 11, Table S7). The higher stability of the complex on comparing with the free probe accounts for the direct influence of Al^{3+} in the electronic structure and energy of the molecular levels of H-PNAP. This conjecture is supported by DFT computation (vide infra).

The selective detection of Al^{3+} by the probe has been appropriated by the intervention of various cations (Figure S25), and it shows that no significant interference is observed. H-PNAP is nonemissive in the wide range of pH (2–12) and the $[\text{Al}(\text{PNAP})(\text{NO}_3)_2]$ emission is untroubled in the pH range 2–11 (Figure S26). The low-intensity emission of the $[\text{Al}(\text{PNAP})(\text{NO}_3)_2]$ complex at a higher pH (pH, 12) may be because of the dissociation of the complex and the formation of $\text{Al}(\text{OH})_3/\text{Al}(\text{OH})_2^-$.

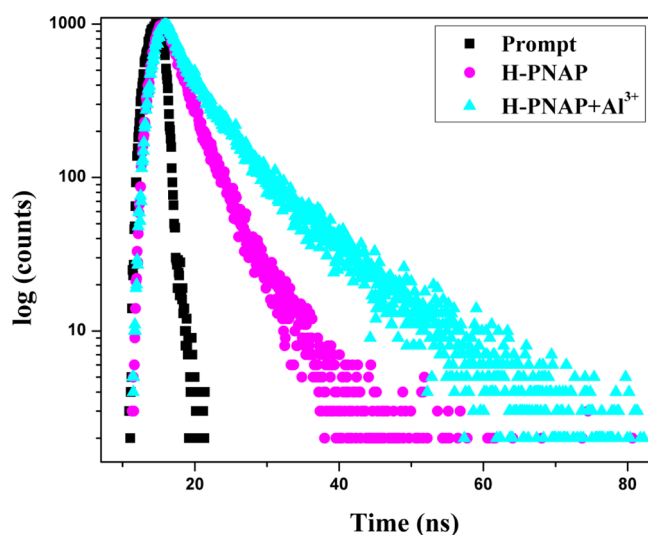
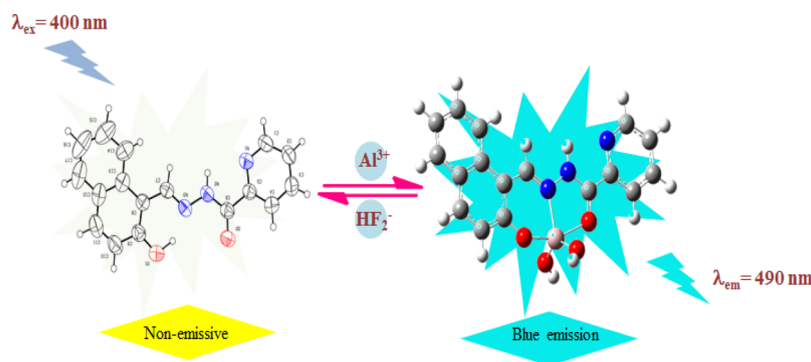


Figure 11. Fluorescence lifetime plot of H-PNAP and $[\text{Al}(\text{PNAP})-(\text{NO}_3)_2]$ in aqueous medium.

The stoichiometry of the complexation of H-PNAP with Al^{3+} is obtained from the spectral titration, Job's plot (Figure S27), which supports the formation of the 1:1 complex. Mass spectral analysis strongly supplements the formation of the 1:1 H-PNAP– Al^{3+} complex (Figure S6) with the molecular ion peak at $m/z = 442.1086$ ($[\text{Al}(\text{PNAP})(\text{NO}_3)_2]$, calculated mass = 442.06). The ^1H NMR titration experiment (Figure S28) displays that upon gradual addition of Al^{3+} , the peak at 12.73 ppm for phenolic OH gradually decreases, and at 1:1 mol ratio it is vanished, but the hydrazide NH peak remains intact. The mechanism for Al^{3+} sensing can be explained by switching OFF the PET and ESIPT processes of free H-PNAP along with switching ON the CHEF process (Scheme S3) on complexation. In the probe, the charge transfer from pyridyl N to the naphthyl ring at the excited state (PET ON) and the ESIPT of H-bonded six-member ring may be the reasons for the nonemissive feature. Upon binding with Al^{3+} , the two above possibilities to the loss of energy are arrested, and CHEF is now ON and PET is OFF along with ESIPT being OFF, which may be accompanied by the remarkable fluorescence emission at 490 nm. The DLS measurement is done for the 1:1 complex for H-PNAP + Al^{3+} , and it is observed that almost no significant difference in average particle size is observed (H-PNAP, 305 nm; H-PNAP + Al^{3+} , 309 nm) (Figure S29). The probe senses Al^{3+} ion in pure water and also some other solvents like MeOH, EtOH, and CH_3CN (emission intensity is lower compared to water) (Figure S30), but out of these solvents, water is green; so, we have performed the ion sensitivity in an aqueous medium. The single probe shows emission at two different wavelengths, one for the AIE emission at 540 nm in a 90% water/MeOH mixture and the other for the $[\text{Al}(\text{PNAP})(\text{NO}_3)_2]$ complex at 490 nm in a pure aqueous medium. Binding of a metal ion to organic fluorogen affects the energy of the states (S_0 , S_1 , ... S_n), and hence the emission energy, polarity, rigidity, relaxation, and so forth of the emitter have changed. Aggregation is normally a physical process and Al^{3+} binding is a chemical process; so, the effects of these processes are certainly different.

According to Pearson's HSAB theory, Al^{3+} is a hard acid, and the hard base centers like O (phenolato, carboxylate, etc.) and N (amine, imine, azo, etc.) may prefer to bind Al^{3+} . The probe

Scheme 3. Ion Sensitivity of H-PNAP in Aqueous Medium



H-PNAP has three potential monoanionic donor centers: O, N, O. Hence, according to the HSAB theory, the probe may favor to coordinate Al^{3+} . There are as many as 25 hard acid centers (H^+ , Li^+ , Na^+ , K^+ , Be^{2+} , Mg^{2+} , Ca^{2+} , Sr^{2+} , Sn^{2+} , Al^{3+} , Ga^{3+} , In^{3+} , Cr^{3+} , Co^{3+} , Fe^{3+} , Ir^{3+} , La^{3+} , Si^{4+} , Ti^{4+} , Zr^{4+} , Th^{4+} , U^{4+} , VO^{2+} , and UO_2^{2+}), whereas the stability of the complex depends on the strength of the binding interaction, charge, chelate ring size, and so forth under experimental conditions. Till date, no theoretical principle has developed to tune the fine experimental preference of donor centers to the metal ions. However, the fluorescence intensity is one of the finest experimental evidences to the preferential binding of the ligand to the metal-ion center. The probe, H-PNAP, is nonemissive in a pure aqueous medium, but becomes highly emissive in the presence of Al^{3+} (λ_{em} , 490 nm) out of 17 other biologically important metal ions. The selective sensing of Al^{3+} is unclear, and it may be explained considering the CHEF process; the hydrated Al^{3+} ion can fit to the cavity of H-PNAP nicely, but other ions may not show such an effect. The binding cavity of the O,N,O pocket may be of such a size to fit nicely on binding Al^{3+} strongly than other ions, and the resulting rigidity imposed on the motif has compelled the excited state to deactivate the radiative process. Other metal ions may have some interaction with H-PNAP, but excited state may dissociate and becomes nonfluorescent. This may be the reason for the other metal ions do not induce fluorescence.

Anion Sensitivity of the $[\text{Al}(\text{PNAP})(\text{NO}_3)_2]$ Complex. The $[\text{Al}(\text{PNAP})(\text{NO}_3)_2]$ complex is highly emissive; hence, the reversibility of emission is checked by adding various anions like $\text{S}_2\text{O}_3^{2-}$, SCN^- , PO_4^{3-} , H_2PO_4^- , HPO_4^{2-} , I^- , OAc^- , ClO_4^- , SO_4^{2-} , HSO_4^- , Cl^- , F^- , HF_2^- , NO_3^- , Br^- , NO_2^- , CN^- , N_3^- , AsO_4^{3-} , and AsO_2^- . In pure water (pH 7.2, HEPES buffer), high-intensity fluorescence emission at 490 nm for $[\text{Al}(\text{PNAP})(\text{NO}_3)_2]$ selectively quenches in the presence of HF_2^- . F^- and PO_4^{3-} also show quenching of emission but much lower than that of HF_2^- (Figure S31). Hence, the in situ-generated $[\text{Al}(\text{PNAP})(\text{NO}_3)_2]$ complex may act as a secondary sensor to bifluoride ion (Scheme 3). There are very rare reports of bifluoride ion sensors till date (Table S8).^{55–57} Hence, our probe is helpful in HF_2^- detection which is very much needed in the present situation. For understanding the privileged mechanism of HF_2^- quenching interaction with $[\text{Al}(\text{PNAP})(\text{NO}_3)_2]$, the spectrofluorimetric titration has been performed by a gradual addition of HF_2^- solution (3 μM each) to the in situ-generated emissive 1:1 $[\text{Al}(\text{PNAP})(\text{NO}_3)_2]$ complex in aqueous solution (pH 7.2, HEPES buffer), and it is observed that the emission intensity gradually decreases (Figure S32).

The UV–vis titration is also performed to authenticate the binding of HF_2^- with the $[\text{Al}(\text{PNAP})(\text{NO}_3)_2]$ complex (Figure S33). It shows that upon incremental addition of HF_2^- to the emissive complex $[\text{Al}(\text{PNAP})(\text{NO}_3)_2]$, the intensity of the band decreases with the generation of new bands. This observation may account for the chemical interaction of HF_2^- with the complex, $[\text{Al}(\text{PNAP})(\text{NO}_3)_2]$, and finally dechelate Al^{3+} . HF_2^- interacts with the $[\text{Al}(\text{PNAP})(\text{NO}_3)_2]$ complex, and to prove the type of interaction, ESI-MS spectra were also collected by the addition of HF_2^- to the in situ-generated solution phase of the $[\text{Al}(\text{PNAP})(\text{NO}_3)_2]$ complex; the mass spectrum displays the intense peak at 292.0915 which corresponds to the free ligand, and after zooming the spectrum from 0 to 280, we get some peaks for various aluminum salts (Figure S34). Few other chelating reagents like the disodium salts of ethylenediaminetetraacetate (Na_2EDTA), 8-hydroxyquinoline (Hoxin), dimethylglyoxime (H_2DMG), 1, 3 diaminoguanidine (1,3 AGUA), and ethylene glycol (EGOH) have been added and the emission intensity is checked (Figure S35). It is observed that the high emission of $[\text{Al}(\text{PNAP})(\text{NO}_3)_2]$ also remains insensitive to them with a small decrement to Na_2EDTA and Hoxin. Thus, selective quenching of an intense emission of $[\text{Al}(\text{PNAP})(\text{NO}_3)_2]$ by HF_2^- may be very useful for the identification of toxic bifluoride.

The proposed mechanism for the selective sensing of HF_2^- may be explained by Scheme S4. It shows that free pyridine N may interact through a hydrogen bond to bring HF_2^- that becomes closer to the Al^{3+} center in the complex, which may be responsible for the possible chemical interaction with Al^{3+} to get removed from the coordination site as the fluoro complex of $\text{Al}(\text{III})$. Hence quenches the emission of the $[\text{Al}(\text{PNAP})(\text{NO}_3)_2]$ complex. The LOD for HF_2^- (3 σ method) is 15 nM (Figure S36). The binding constant K_d (HF_2^-), $1.3 \times 10^4 \text{ M}^{-1}$, is calculated by using the Benesi–Hildebrand plot (Figure S37).

Theoretical Evaluation of Spectroscopic Data. DFT computation is managed to obtain the optimized structure of H-PNAP and Al^{3+} –H-PNAP $[\text{Al}(\text{PNAP})(\text{OH})_2]$ as a model complex (Figure S38). The single crystal X-ray crystallographic parameters are used for H-PNAP. The metric parameters obtained from the crystal structure and the theoretically determined structure are in good agreement with the X-ray structure, bond length (\AA), calc. (expt): $\text{C}=\text{O}$ 1.24 (1.23), $\text{C}=\text{N}$ 1.30 (1.28), $\text{C}-\text{N}$ 1.37 (1.34) $\text{N}-\text{N}$ 1.37 (1.37) $\text{C}-\text{O}$ 1.36 (1.34). For the interpretation of the theoretical facets of the observed spectroscopic responses of H-PNAP toward Al^{3+} , TDDFT is also performed. The frontier molecular orbital

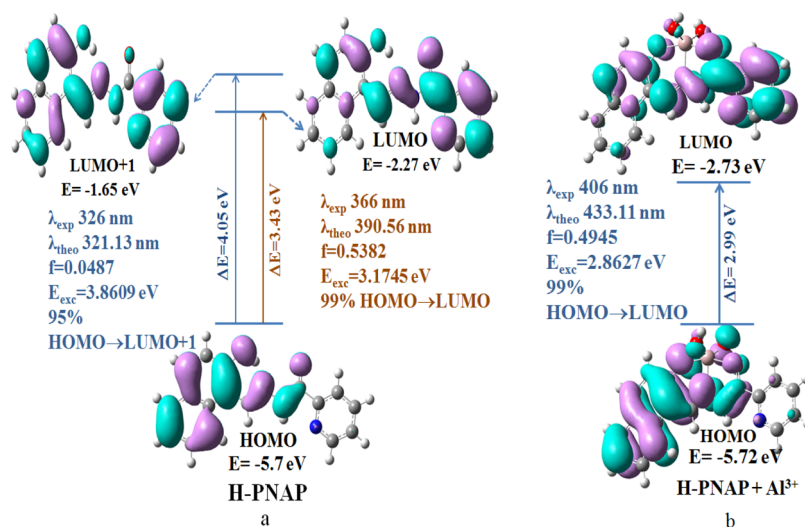


Figure 12. Probable electronic transitions and relationship between UV-vis experimental measurement and theoretical (TDDFT) calculation of (a) H-PNAP and (b) [Al(PNAP)(OH)₂].

images with the energy and orbital contributions of H-PNAP (Table S9, Figure S39) and [Al(PNAP)(OH)₂] (Table S10, Figure S40) are shown. The possible electronic transitions for the probe and its Al complex are interpreted by TDDFT (Tables S11 and S12). Some selected bond lengths of the [Al(PNAP)(OH)₂] complex obtained from the optimized structure are: bond length (Å): Al–OH (1.74), C=O (1.27), Al–N (2.06), Al–O (1.87), and Al–O (of C=O, 2.1). In the UV-vis spectrum in pure aqueous media, the probe shows two sharp bands at 326 and 366 nm which correspond to the highest occupied molecular orbital (HOMO) \rightarrow lowest occupied molecular orbital (LUMO) + 1 and HOMO \rightarrow LUMO transitions, respectively (obtained from DFT calculations), and also a broad band at 440 nm (Figure 12a); for its Al complex, a new band appears at 406 nm in the UV-vis spectra (Figure S22), which may be because of the HOMO \rightarrow LUMO transition. The HOMO–LUMO gap in H-PNAP is 3.43 eV, and upon coordination with Al³⁺, this gap changes to 2.99 eV, which supports the shifting of λ_{max} in the UV-vis absorption spectrum, and is represented by the schematic MO diagram (Figure 12b).

Applications: Recovery Study for Al³⁺ from Municipal Supplied Water Sample. To evaluate the reliability of the fluorescence detection method for Al³⁺, a recovery study of Al³⁺ from drinking water sample (Kolkata Municipal Supplied water in Jadavpur University Campus) has been performed by a standard addition method. The fluorescence emission intensity is measured at 490 nm upon excitation at 400 nm for the calibration plot by varying the concentration of Al³⁺ ion from 1 to 10 μM by maintaining the concentration of probe at 10 μM in pure H₂O (HEPES buffer, pH 7.2) (Figure S41). From the calibration plot, an unknown concentration of Al³⁺ is measured (Table 1). A satisfactory result for the recovery of Al³⁺ from drinking water sample is obtained. This testing has exhibited a pleasing, rapid, and inexpensive application of the probe, H-PNAP, for the Al³⁺ ion for on-demand water analysis.

Paper Strip Detection Kits. The probe shows distinct emission in an aggregated state (9:1 H₂O/MeOH) and in the presence of Al³⁺ (in pure water) at 540 and 490 nm, respectively. A potential application may be assisted by this single probe as an accessible transportable tool for sensing

Table 1. Recovery of Al³⁺ Ions in Drinking Water Samples Using the Probe H-PNAP

sample	added Al ³⁺ (μM)	emission intensity, 490 nm (a.u.)	experimentally Found Al ³⁺ (μM)	recovery (%)
drinking water	2	91	1.69	84.5
	4	157	3.69	92.2
	6	209	5.22	87.0

TNP/DNP and Al³⁺. We have prepared a test paper strip by dip-coating a solution of H-PNAP (10 μM) in 90% water in MeOH onto a Whatman 41 filter paper. The dried paper strip is soaked in 30 μM solution of TNP/DNP, dried, and then images are taken under a UV lamp at 365 nm. The green emission of the aggregated probe quenches in the presence of TNP/DNP (Figure 13). For Al³⁺ sensing in paper strip, we

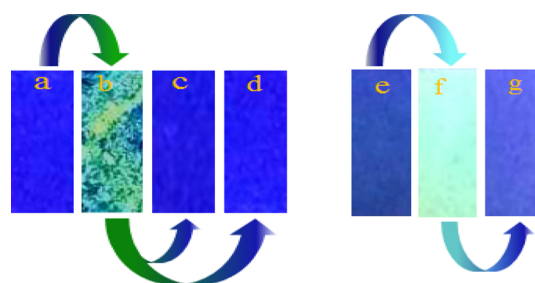
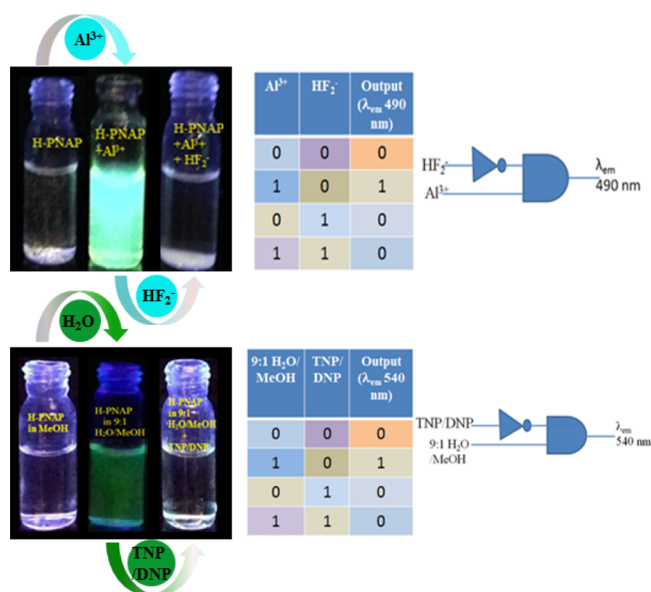


Figure 13. Detection of TNP/DNP by the test strip method under UV lamp (365 nm): probe in pure MeOH (a), 9:1 H₂O/MeOH (b), in the presence of DNP (c), and TNP (d). Detection of Al³⁺ and HF₂⁻ by the test strip method under UV lamp (365 nm): probe in H₂O (e), in the presence of Al³⁺ (f) and Al³⁺ + HF₂⁻ (g).

prepared test paper strips by dip-coating a solution of H-PNAP (10 μM) in pure water on a Whatmann 41 filter paper, and then this paper strip was dipped in 10 μM of Al³⁺ solution, dried, and images were taken under a UV lamp (365 nm). Again, this Al³⁺-coated paper was dipped in a 20 μM solution of HF₂⁻, and images were taken after drying (Figure 13). In the presence of Al³⁺, the probe shows blue emission, but upon treatment with HF₂⁻, this high emission is quenched.

Application in Logic Gate. A single molecule that has light sensitivity is very much beneficial for the construction of integrated logic gates like full-adder, half-adder, full-subtractor, half-subtractor, and INHIBIT.⁵⁸ The probe in pure methanol has no emission, but in 9:1 H₂O/MeOH medium it has generated a new emission band at 540 nm. This highly emissive aggregated probe selectively quenches in the presence of TNP/DNP. Hence, the probe undergoes turn-on emission in the 9:1 H₂O/MeOH medium and turns off in the presence of TNP or DNP. Therefore, with the two chemical inputs 9:1 H₂O/MeOH and TNP/DNP, H-PNAP can develop a logic gate (INHIBIT). Not only can the probe construct an INHIBIT logic gate for inputs such as 9:1 H₂O/MeOH and TNP/DNP, but it can also build another logic gate by the chemical inputs Al³⁺ and HF₂[−] because in the presence of Al³⁺ in pure water the probe shows high emission at 490 nm, and this emission is selectively quenched by HF₂[−] (Scheme 4).

Scheme 4. Molecular Logic Gate (INHIBIT) Construction by Al³⁺–HF₂[−] and 9:1 H₂O/MeOH–(TNP/DNP)



Living Cell Imaging. The in vitro cytotoxicity of the probe, H-PNAP, is estimated for checking the biocompatibility of WI38 cell line. The cells were treated with five different concentrations (20, 40, 60, 80, and 100 μM/mL) of ligand for 24 h, followed by MTT assay (Figure 14). It is observed that the ligand exhibited no significant toxicities even at the highest concentration of 100 μM. Therefore, the ligand shows good biocompatibility and is beneficial for biological applications.

The fluorescence microscopic study is performed to envisage the cellular uptake of the probe H-PNAP (5 μM) and Al³⁺ salt (10 μM). A prominent blue fluorescent signal is observed under the microscope. After the addition of HF₂[−] salt (10 μM), the fluorescent signal immediately disappears (Figure 15). From this observation, it is concluded that the cells readily uptake the probe H-PNAP and the Al³⁺ salt which results in a blue fluorescent signal, and the signal immediately quenches after the addition of the HF₂[−] salt. Hence, H-PNAP is not only an ion sensor, but has multiple applications and has successfully been applied in the detection of intracellular Al³⁺ and HF₂[−] in the MDA-MB-468 cell and shows better efficiency with respect to other reported ligands (Table S13).^{59–69}

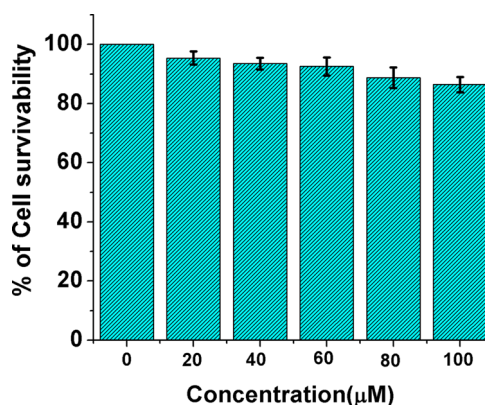


Figure 14. Cell survivability study of WI38 cells exposed to H-PNAP.

CONCLUSIONS

An AIE-active fluorescence probe, (*E*)-*N*'-((2-hydroxynaphthalen-1-yl)methylene)picolinohydrazide (H-PNAP), has been characterized and used for sensing of NACs (TNP and DNP with LOD ~0.8 and 0.9 μM, respectively) in a 90% water/MeOH medium. The aqueous solution of the probe is highly selective and sensitive to Al³⁺ (LOD, 2.09 nM) which serves as a secondary sensor to HF₂[−] (LOD, 15 nM). For practical applicability of the probe (H-PNAP), a recovery study of Al³⁺ from drinking water sample has been done. H-PNAP builds the INHIBIT logic gate with two chemical inputs Al³⁺, HF₂[−] and 90% H₂O/MeOH, TNP/DNP. Moreover, H-PNAP has the capability to be visible, practical, and speedy to monitor Al³⁺ and nitroexplosives (TNP/DNP) by simple paper test strips. The probe H-PNAP is used to detect Al³⁺, and the resulting emissive complex [Al(PNAP)(NO₃)₂] identifies HF₂[−] ions in live cells (MDA-MB-468).

EXPERIMENTAL SECTION

Materials and Methods. All organic and inorganic chemicals were purchased from Merck except 2-picolinic acid (High-Media) and used without further purification. Water for aqueous solutions was obtained from Millipore water (Milli-Q). Elemental analyses (C, H and N) were performed using a PerkinElmer 2400 Series-II CHN analyzer, USA elemental analyzer. The fluorescence spectra were recorded using a PerkinElmer spectrofluorimeter model LS55, UV–vis spectra were obtained from PerkinElmer Lambda 25 spectrophotometer, and the time-resolved single-photon counting measurements were carried out by using time-correlated single-photon counting setup from HORIBA Jobin-Yvon; Fourier transform infrared (FT-IR) spectra were recorded from a PerkinElmer LX-1 FT-IR spectrophotometer (KBr disk, 4000–400 cm^{−1}). All the required NMR spectra were obtained from a Bruker (AC) 500 MHz FT-NMR spectrometer using trimethylsilane (TMS) as an internal standard. ESI mass spectra were recorded from a Water HRMS model XEVO-G2QTOF#Y-CA351 spectrometer. All of the measurements were carried out at room temperature.

Synthesis of H-PNAP. Picolinohydrazide was prepared from 2-picolinic acid following the reported procedure.⁷⁰ Picolinohydrazide (137 mg, 1.0 mmol) was added to 2-hydroxy-1-naphthaldehyde (172 mg, 1.0 mmol) in dry MeOH (15 mL) and stirred for 6 h, and a greenish yellow solution was obtained. Then, this solution was kept in air and allowed to evaporate slowly. After few days (2 weeks), yellow crystals of

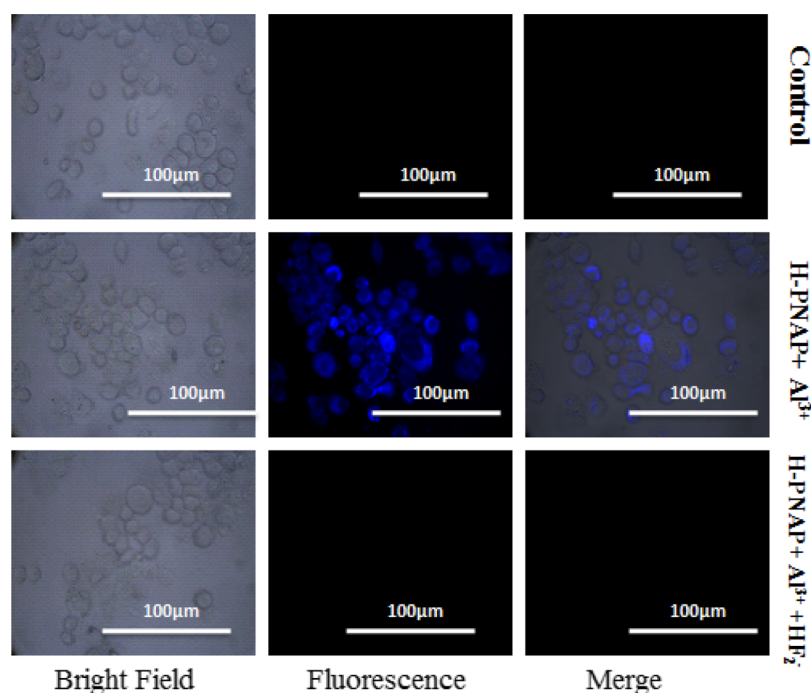


Figure 15. Bright-field, fluorescence, and merged microscopic images of untreated MDA-MB-468 (control); cells treated with H-PNAP (5 μ M) + Al^{3+} (10 μ M) and with H-PNAP (5 μ M) + Al^{3+} (10 μ M) + HF_2^- (10 μ M).

H-PNAP were obtained. Then, the crystals were collected from the solvent and dried in open air (yield, 89%), mp 186 $^{\circ}\text{C}$ (Scheme S1). Microanalytical data: $\text{C}_{17}\text{H}_{13}\text{N}_3\text{O}_2$ calcd (found): C, 70.09 (69.55); H, 4.50 (4.54); N, 14.42 (13.85) %. ^1H NMR (500 MHz, $\text{DMSO}-d_6$) (δ , ppm): 12.73 (s, 1H, $-\text{OH}$), 12.387 (s, 1H, $-\text{NH}$), 9.628 (s, 1H, imine-H), 8.573–8.582 (d, 1H), 7.976–8.010 (t, 2H), 7.899–7.917 (dd, 1H), 7.740–7.758 (d, 1H), 7.699–7.715 (d, 1H), 7.507–7.531 (dd, 1H), 7.404–7.434 (t, 1H), 7.205–7.234 (t, 1H), 7.034–7.052 (d, 1H) (Figure S1); ^{13}C NMR (in $\text{DMSO}-d_6$) (δ , ppm): 160.49, 158.63, 149.41, 149.15, 149.04, 138.65, 133.34, 132.33, 129.45, 128.27, 128.24, 127.49, 124.06, 123.30, 120.99, 119.43, 108.99 (Figure S2); The ESI-MS peak for H-PNAP at 292.1084 (calculated mass for H-PNAP + H^+ , 292.11) corresponds to $[\text{M} + \text{H}^+]$ and the base peak at 314.0985 for $[\text{M} + \text{Na}^+]$ (Figure S3); FT-IR for H-PNAP: ν 3482 cm^{-1} (OH), ν 3191 cm^{-1} (NH), ν 1661 cm^{-1} (C=O), ν 1620 cm^{-1} (C=N) (Figure S4).

Single-Crystal X-ray Crystallographic Measurement of H-PNAP. Slow evaporation of MeOH solution had a crystallized yellow prism ($0.145 \times 0.089 \times 0.045 \text{ mm}^3$) of H-PNAP. The crystal data and data collection (Table S1) were carried out using an X-ray diffraction instrument of Bruker Smart APEX II CCD Area Detector at 296(2) K. Graphite-monochromatized Mo $\text{K}\alpha$ radiation of wavelength 0.71073 \AA was used in a fine-focus sealed tube in the hkl range $-6 \leq h \leq 6$; $-29 \leq k \leq 29$; $-17 \leq l \leq 17$ and of angular range $1.796 \leq \theta \leq 27.101^{\circ}$ for data collection. The intensity was corrected, and empirical absorption corrections were considered for Lorentz and polarization effects under the condition of $I > 2\sigma(I)$. The direct method using successive Fourier and difference Fourier syntheses was employed for the structure solution of the crystal. All the nonhydrogen atoms were refined anisotropically and the hydrogen atoms were refined by a riding model. The hydrogen atoms were static geometrically. All these calculations were carried out using ORTEP-32,⁷¹ SHELXL-97,⁷²

and PLATON-99,⁷³ programs. The crystal data of H-PNAP have been deposited to Cambridge Crystallographic Data Centre with CCDC number 1873384.

Theoretical Computation. For the optimization of the ligand and all the complexes, DFT/B3LYP method by Gaussian 09 software was used.⁷⁴ The basis set used for the probe H-PNAP was 6-311+G(d) and that for its Al^{3+} complex was LANL2DZ. Vibrational frequency calculations were performed for confirmation that the optimized geometries represent the local minima, and these only yielded positive eigenvalues. TDDFT was also performed by the use of CPCM;^{75–77} from this, theoretical UV–vis spectral transitions are observed. The fraction of contributions of various groups in each molecular orbital was calculated by carrying out GAUSSSUM.⁷⁸

■ ASSOCIATED CONTENT

§ Supporting Information

The Supporting Information is available free of charge on the ACS Publications website at DOI: 10.1021/acsomega.9b00369.

Comprehensive experimental details such as synthesis and solution preparation for measurements, spectral characterization figures (ESI–MS, NMR, and FT-IR), and X-ray crystallographic data of H-PNAP along with additional required spectra (PDF)

Accession Codes

CCDC number 1873384 contains the crystallographic data of [H-PNAP]. The copies of this data may be picked up free of cost from the Director, CCDC, 12 Union Road, Cambridge CB2 1EZ, UK (e-mail: deposit@ccdc.cam.ac.uk or www: http:// www.ccdc.cam.ac.uk).

AUTHOR INFORMATION

Corresponding Author

*E-mail: crsjuchem@gmail.com.

ORCID

Chittaranjan Sinha: 0000-0002-4537-0609

Funding

The research scheme is funded by the Council of Scientific and Industrial Research (sanction no. 01(2894)/17/EMR-II), New Delhi, India.

Notes

The authors declare no competing financial interest.

ACKNOWLEDGMENTS

The authors thank Jadavpur University for infrastructural support and Council of Scientific and Industrial Research (CSIR, sanction no. 01(2894)/17/EMR-II), New Delhi, for finance. S.D. and R.P. are obliged to the Council of Scientific and Industrial Research (CSIR), Govt. of India, and Department of Science and Technology (DST), Govt. of India, respectively, for the research fellowship.

REFERENCES

- (1) Lippard, S. J.; Berg, J. M. *Principles of Bioinorganic Chemistry*; University Science Books: New York, 1994.
- (2) Crichton, R. *Biological Inorganic Chemistry*, 3rd ed.; Academic Press, 2018.
- (3) (a) Darbre, P. D.; Bakir, A.; Iskakova, E. Effect of aluminium on migratory and invasive properties of MCF-7 human breast cancer cells in culture. *J. Inorg. Biochem.* **2013**, *128*, 245–249. (b) Rondeau, V.; Commenges, D.; Jacqmin-Gadda, H.; Dartigues, J.-F. Relation between aluminum concentrations in drinking water and Alzheimer's disease: an 8-year follow-up study. *Am. J. Epidemiol.* **2000**, *152*, 59–66.
- (4) Darbre, P. D.; Mannello, F.; Exley, C. Aluminium and breast cancer: Sources of exposure, tissue measurements and mechanisms of toxicological actions on breast biology. *J. Inorg. Biochem.* **2013**, *128*, 257–261.
- (5) (a) Meng, Q.; Liu, H.; Sen, C.; Cao, C.; Ren, J. A novel molecular probe sensing polynuclear hydrolyzed aluminum by chelation-enhanced fluorescence. *Talanta* **2012**, *99*, 464–470. (b) Kaur, K.; Bhardwaj, V. K.; Kaur, N.; Singh, N. Imine linked fluorescent chemosensor for Al^{3+} and resultant complex as a chemosensor for HSO_4^- anion. *Inorg. Chem. Commun.* **2012**, *18*, 79–82. (c) Liao, Z.-C.; Yang, Z.-Y.; Li, Y.; Wang, B.-D.; Zhou, Q.-X. A simple structure fluorescent chemosensor for high selectivity and sensitivity of aluminum ions. *Dyes Pigm.* **2013**, *97*, 124–128. (d) Li, Y.-P.; Liu, X.-M.; Zhang, Y.-H.; Chang, Z. A fluorescent and colorimetric sensor for Al^{3+} based on a dibenzo-18-crown-6 derivative. *Inorg. Chem. Commun.* **2013**, *33*, 6–9.
- (6) (a) Alyaninezhad, Z.; Bekhradnia, A.; Feizi, N.; Arshadi, S.; Zibandeh, M. A novel aluminum-sensitive fluorescent chemosensor based on 4-aminoantipyrine: An experimental and theoretical study. *Spectrochim. Acta, Part A* **2019**, *212*, 32–41. (b) Selvan, G. T.; Poomalai, S.; Ramasamy, S.; Selvakumar, P. M.; Muthu Vijayan Enoch, I. V.; Lanas, S. G.; Melchior, A. Differential Metal Ion Sensing by an Antipyrine Derivative in Aqueous and β -Cyclodextrin Media: Selectivity Tuning by β -Cyclodextrin. *Anal. Chem.* **2018**, *90*, 13607–13615.
- (7) (a) Yu, M.; Yuan, R.; Shi, C.; Zhou, W.; Wei, L.; Li, Z. 1, 8-naphthyridine and 8-hydroxyquinoline modified Rhodamine B derivatives: "Turn-on" fluorescent and colorimetric sensors for Al^{3+} and Cu^{2+} . *Dyes Pigm.* **2013**, *99*, 887–894. (b) Manjunath, R.; Kannan, P. Highly selective rhodamine-based fluorescence turn-on chemosensor for Al^{3+} ion. *Opt. Mater.* **2018**, *79*, 38–44. (c) Mabhai, S.; Dolai, M.; Dey, S.; Dhara, A.; Das, B.; Jana, A. A novel chemosensor based on rhodamine and azobenzene moieties for selective detection of Al^{3+} ions. *New J. Chem.* **2018**, *42*, 10191–10201. (d) Maniyazagan, M.; Mariadasse, R.; Nachiappan, M.; Jeyakanthan, J.; Lokanath, N. K.; Naveen, S.; Sivaraman, G.; Muthuraja, P.; Manisankar, P.; Stalin, T. Synthesis of rhodamine based organic nanorods for efficient chemosensor probe for Al (III) ions and its biological applications. *Sens. Actuators, B* **2018**, *254*, 795–804. (e) Li, C.-Y.; Zhou, Y.; Li, Y.-F.; Zou, C.-X.; Kong, X.-F. Efficient FRET-based colorimetric and ratiometric fluorescent chemosensor for Al^{3+} in living cells. *Sens. Actuators, B* **2013**, *186*, 360–366. (f) Maity, S. B.; Bharadwaj, P. K. A Chemosensor Built with Rhodamine Derivatives Appended to an Aromatic Platform via 1,2,3-Triazoles: Dual Detection of Aluminum-(III) and Fluoride/Acetate Ions. *Inorg. Chem.* **2013**, *52*, 1161–1163. (g) Jeong, J. W.; Rao, B. A.; Lee, J.-Y.; Hwang, J.-Y.; Son, Y.-A. An "OFF-ON" fluorescent chemosensor based on rhodamine 6G-2-chloronicotinaldehyde for the detection of Al^{3+} ions: Part II. *Sens. Actuators, B* **2016**, *227*, 227–241. (h) Gupta, V. K.; Mergu, N.; Kumawat, L. K.; Singh, A. K. A reversible fluorescence "off-on-off" sensor for sequential detection of aluminum and acetate/fluoride ions. *Talanta* **2015**, *144*, 80–89.
- (8) (a) Wang, L.; Li, H.; Cao, D. A new photoresponsive coumarin-derived Schiff base: Chemosensor selectively for Al^{3+} and Fe^{3+} and fluorescence "turn-on" under room light. *Sens. Actuators, B* **2013**, *181*, 749–755. (b) Cao, L.; Jia, C.; Huang, Y.; Zhang, Q.; Wang, N.; Xue, Y.; Du, D. A highly selective fluorescence turn-on detection of Al^{3+} and Ca^{2+} based on a coumarin-modified rhodamine derivative. *Tetrahedron Lett.* **2014**, *55*, 4062–4066. (c) Sarkar, D.; Ghosh, P.; Gharami, S.; Mondal, T. K.; Murmu, N. A novel coumarin based molecular switch for the sequential detection of Al^{3+} and F^- : Application in lung cancer live cell imaging and onstruction of logic gate. *Sens. Actuators, B* **2017**, *242*, 338–346. (d) Hossain, S. M.; Singh, K.; Lakma, A.; Pradhan, R. N.; Singh, A. K. A schiff base ligand of coumarin derivative as an ICT-Based fluorescence chemosensor for Al^{3+} . *Sens. Actuators, B* **2017**, *239*, 1109–1117. (e) Yan, L.-Q.; Cui, M.-F.; Zhou, Y.; Ma, Y.; Qi, Z.-J. A Simplified and turn-on fluorescence chemosensor based on coumarin derivative for detection of aluminium(III) ion in pure aqueous solution. *Anal. Sci.* **2015**, *31*, 1055–1059. (f) Qin, J.-c.; Li, T.-r.; Wang, B.-d.; Yang, Z.-y.; Fan, L. Fluorescent sensor for selective detection of Al^{3+} based on quinoline-coumarin conjugate. *Spectrochim. Acta, Part A* **2014**, *133*, 38–43.
- (9) (a) Sinha, S.; Koner, R. R.; Kumar, S.; Mathew, J.; Monisha, P. V.; Kazi, I.; Ghosh, S. Imine containing benzophenone scaffold as an efficient chemical device to detect selectively Al^{3+} . *RSC Adv.* **2013**, *3*, 345–351. (b) Maity, D.; Govindaraju, T. Conformationally Constrained (Coumarin-Triazolyl-Bipyridyl) Click Fluoroionophore as a Selective Al^{3+} -Sensor. *Inorg. Chem.* **2010**, *49*, 7229–7231. (c) Naskar, B.; Modak, R.; Sikdar, Y.; Maiti, D. K.; Bauzá, A.; Frontera, A.; Katarkar, A.; Chaudhuri, K.; Goswami, S. Fluorescent sensing of Al^{3+} by benzophenone based Schiff base chemosensor and live cell imaging applications: Impact of keto-enol tautomerism. *Sens. Actuators, B* **2017**, *239*, 1194–1204.
- (10) (a) Liu, C.; Yang, Z.; Yan, M. A highly selective and sensitive fluorescent turn-on chemosensor for Al^{3+} based on a chromone Schiff base. *J. Coord. Chem.* **2012**, *65*, 3845–3850. (b) Fan, L.; Li, T.-r.; Wang, B.-d.; Yang, Z.-y.; Liu, C.-j. A colorimetric and turn-on fluorescent chemosensor for Al(III) based on a chromone Schiff-base. *Spectrochim. Acta, Part A* **2014**, *118*, 760–764. (c) Fan, L.; Qin, J.-c.; Li, T.-r.; Wang, B.-d.; Yang, Z.-y. A chromone Schiff-base as Al(III) selective fluorescent and colorimetric chemosensor. *J. Lumin.* **2014**, *155*, 84–88. (d) Liu, C.-j.; Yang, Z.-y.; Fan, L.; Jin, X.-l.; An, J.-m.; Cheng, X.-y.; Wang, B.-d. Novel optical selective chromone Schiff base chemosensor for Al^{3+} ion. *J. Lumin.* **2015**, *158*, 172–175.
- (11) (a) Han, T.; Feng, X.; Tong, B.; Shi, J.; Chen, L.; Zhi, J.; Dong, Y. A novel "turn-on" fluorescent chemosensor for the selective detection of Al^{3+} based on aggregation-induced emission. *Chem. Commun.* **2012**, *48*, 416–418. (b) Mal, K.; Naskar, B.; Mondal, A.; Goswami, S.; Prodhan, C.; Chaudhuri, K.; Mukhopadhyay, C. Dihydroindeno[1, 2-: B] pyrroles: New Al^{3+} selective off-on chemosensors for bio-imaging in living HepG2 cells. *Org. Biomol. Chem.* **2018**, *16*, 5920–5931. (c) Shree, G. J.; Sivaraman, G.; Siva, A.;

Chellappa, D. Anthracene- and pyrene-bearing imidazoles as turn-on fluorescent chemosensor for aluminum ion in living cells. *Dyes Pigm.* **2019**, *163*, 204–212.

(12) (a) Kong, X.-y.; Hou, L.-J.; Shao, X.-q.; Shuang, S.-M.; Wang, Y.; Dong, C. A phenolphthalein-based fluorescent probe for the sequential sensing of Al^{3+} and F^- ions in aqueous medium and live cells. *Spectrochim. Acta, Part A* **2019**, *208*, 131–139. (b) Zhang, S. J.; Li, H.; Gong, C. L.; Wang, J. Z.; Wu, Z. Y.; Wang, F. Novel 4,5-diazafluorene-based Schiff base derivatives as Al^{3+} ions fluorescence turn-on sensors. *Synth. Met.* **2016**, *217*, 37–42. (c) Gao, W.; Zhang, Y.; Li, H.; Pu, S. A multi-controllable selective fluorescent turn-on chemosensor for Al^{3+} and Zn^{2+} based on a new diarylethene with a 3-(4-methylphenyl)-1H-pyrazol-5-amine Schiff base group. *Tetrahedron* **2018**, *74*, 6299–6309. (d) Naskar, B.; Das, K.; Mondal, R. R.; Maiti, D. K.; Requena, A.; Cerón-Carrasco, J. P.; Prodhan, C.; Chaudhuri, K.; Goswami, S. A new fluorescence turn-on chemosensor for nanomolar detection of Al^{3+} constructed from a pyridine-pyrazole system. *New J. Chem.* **2018**, *42*, 2933–2941. (e) Rangasamy, M.; Palaninathan, K. A pyrazoline-based fluorescent chemosensor for Al^{3+} ion detection and live cell imaging. *New J. Chem.* **2018**, *42*, 10891–10897.

(13) (a) Singh, R.; Samanta, S.; Mullick, P.; Ramesh, A.; Das, G. Al^{3+} sensing through different turn-on emission signals vis-à-vis two different excitations: Applications in biological and environmental realms. *Anal. Chim. Acta* **2018**, *1025*, 172–180. (b) Hazra, A.; Roy, A.; Mukherjee, A.; Maiti, G. P.; Roy, P. Remarkable difference in Al^{3+} and Zn^{2+} sensing properties of quinoline based isomers. *Dalton Trans.* **2018**, *47*, 13972–13989. (c) Huang, C.-Y.; Jhong, Y.; Chir, J.-L.; Wu, A.-T. A quinoline derivative as an efficient sensor to detect selectively Al^{3+} ion. *J. Fluoresc.* **2014**, *24*, 991–994. (d) Anand, T.; Sivaraman, G.; Mahesh, A.; Chellappa, D. Aminoquinoline based highly sensitive fluorescent sensor for lead(II) and aluminum(III) and its application in live cell imaging. *Anal. Chim. Acta* **2015**, *853*, 596–601. (e) Fan, L.; Jiang, X.-h.; Wang, B.-d.; Yang, Z.-y. 4-(8'-Hydroxyquinolin-7'-yl)methyleneimino-1-phenyl-2,3-dimethyl-5-pyazole as a fluorescent chemosensor for aluminum ion in acid aqueous medium. *Sens. Actuators, B* **2014**, *205*, 249–254. (f) Lashgari, N.; Badieli, A.; Mohammadi Ziarani, G. A Fluorescent Sensor for $\text{Al}(\text{III})$ and Colorimetric Sensor for $\text{Fe}(\text{III})$ and $\text{Fe}(\text{II})$ Based on a Novel 8-Hydroxyquinoline Derivative. *J. Fluoresc.* **2016**, *26*, 1885–1894.

(14) (a) Tajbakhsh, M.; Chalmardi, G. B.; Bekhradnia, A.; Hosseinzadeh, R.; Hasani, N.; Amiri, M. A. A new fluorene-based Schiff-base as fluorescent chemosensor for selective detection of Cr^{3+} and Al^{3+} . *Spectrochim. Acta, Part A* **2018**, *189*, 22–31. (b) Wu, C.-S.; Lin, Y.-J.; Chen, Y. A fluorene-based material containing triple azacrown ether groups: Synthesis, characterization and application in chemosensors and electroluminescent devices. *Org. Biomol. Chem.* **2014**, *12*, 1419–1429.

(15) (a) Liu, H.; Zhang, B.; Tan, C.; Liu, F.; Cao, J.; Tan, Y.; Jiang, Y. Simultaneous bioimaging recognition of Al^{3+} and Cu^{2+} in living-cell, and further detection of F^- and S^{2-} by a simple fluorogenic benzimidazole-based chemosensor. *Talanta* **2016**, *161*, 309–319. (b) Jeyanthi, D.; Iniya, M.; Krishnaveni, K.; Chellappa, D. A ratiometric fluorescent sensor for selective recognition of Al^{3+} ions based on a simple benzimidazole platform. *RSC Adv.* **2013**, *3*, 20984–20989.

(16) (a) Kumar, G.; Paul, K.; Luxami, V. Aggregation induced emission-excited state intramolecular proton transfer based “off-on” fluorescent sensor for Al^{3+} ions in liquid and solid state. *Sens. Actuators, B* **2018**, *263*, 585–593. (b) Na, N.; Wang, F.; Huang, J.; Niu, C.; Yang, C.; Shang, Z.; Han, F.; Ouyang, J. An aggregation-induced emission-based fluorescent chemosensor of aluminium ions. *RSC Adv.* **2014**, *4*, 35459–35462. (c) Peng, L.; Zhou, Z.; Wang, X.; Wei, R.; Li, K.; Xiang, Y.; Tong, A. A ratiometric fluorescent chemosensor for Al^{3+} in aqueous solution based on aggregation-induced emission and its application in live-cell imaging. *Anal. Chim. Acta* **2014**, *829*, 54–59. (d) Lu, N.; Jiang, T.; Tan, H.; Hang, Y.; Yang, J.; Wang, J.; Qu, X.; Hua, J. A red fluorescent turn-on chemosensor for Al^{3+} based on a dimethoxy triphenylamine

benzothiadiazole derivative with aggregation-induced emission. *Anal. Methods* **2017**, *9*, 2689–2695.

(17) (a) Sen, S.; Mukherjee, T.; Chattopadhyay, B.; Moirangthem, A.; Basu, A.; Marek, J.; Chattopadhyay, P. A water soluble Al^{3+} selective colorimetric and fluorescent turn-on chemosensor and its application in living cell imaging. *Analyst* **2012**, *137*, 3975–3981. (b) Qin, J.-C.; Yan, J.; Wang, B.-d.; Yang, Z.-y. Rhodamine-naphthalene conjugate as a novel ratiometric fluorescent probe for recognition of Al^{3+} . *Tetrahedron Lett.* **2016**, *57*, 1935–1939. (c) Gupta, V. K.; Shoor, S. K.; Kumawat, L. K.; Jain, A. K. A highly selective colorimetric and turn-on fluorescent chemosensor based on 1-(2-pyridylazo)-2-naphthol for the detection of aluminium(III) ions. *Sens. Actuators, B* **2015**, *209*, 15–24. (d) Zhou, D.; Sun, C.; Chen, C.; Cui, X.; Li, W. Research of a highly selective fluorescent chemosensor for aluminum(III) ions based on photoinduced electron transfer. *J. Mol. Struct.* **2015**, *1079*, 315–320. (e) Xiao, N.; Xie, L.; Zhi, X.; Fang, C.-J. A naphthol-based highly selective fluorescence turn-on and reversible sensor for $\text{Al}(\text{III})$ ion. *Inorg. Chem. Commun.* **2018**, *89*, 13–17. (f) Singha, D. K.; Mahata, P. Highly Selective and Sensitive Luminescence Turn-On-Based Sensing of Al^{3+} Ions in Aqueous Medium Using a MOF with Free Functional Sites. *Inorg. Chem.* **2015**, *54*, 6373–6379.

(18) (a) Wu, Y.-P.; Rahman, F.-U.; Bhatti, M. Z.; Yu, S.-B.; Yang, B.; Wang, H.; Li, Z.-T.; Zhang, D.-W. Acylhydrazide as a novel “off-On-Off” fluorescence probe for the sequential detection of Al^{3+} and F^- . *New J. Chem.* **2018**, *42*, 14978–14985. (b) Liao, Z.; Liu, Y.; Han, S.-F.; Wang, D.; Zheng, J.-Q.; Zheng, X.-J.; Jin, L.-P. A novel acylhydrazide-based derivative as dual-mode chemosensor for Al^{3+} , Zn^{2+} and Fe^{3+} and its applications in cell imaging. *Sens. Actuators, B* **2017**, *244*, 914–921. (c) Ma, J.; Shi, W.; Feng, L.; Chen, Y.; Fan, K.; Hao, Y.; Hui, Y.; Xie, Z. A highly selective and sensitive acylhydrazide-based turn-on optical sensor for Al^{3+} . *RSC Adv.* **2016**, *6*, 28034–28037. (d) Kejik, Z.; Kaplánek, R.; Havlík, M.; Bříza, T.; Vavřínová, D.; Dolenský, B.; Martásek, P.; Král, V. Aluminium(III) sensing by pyridoxal hydrazone utilising the chelation enhanced fluorescence effect. *J. Lumin.* **2016**, *180*, 269–277.

(19) Zhang, X.; Wang, R.; Liu, G.; Fan, C.; Pu, S. A highly selective fluorescence probe for Al^{3+} based on a new diarylethene with a 6-(hydroxymethyl)picolinohydrazide unit. *Tetrahedron* **2016**, *72*, 8449–8455.

(20) Gale, P. A.; Caltagirone, C. Anion sensing by small molecules and molecular ensembles. *Chem. Soc. Rev.* **2015**, *44*, 4212–4227.

(21) Salinas, Y.; Martínez-Mañez, R.; Marcos, M. D.; Sancenón, F.; Costero, A. M.; Parra, M.; Gil, S. Optical chemosensors and reagents to detect explosives. *Chem. Soc. Rev.* **2012**, *41*, 1261–1296.

(22) Toal, S. J.; Trogler, W. C. Polymer sensors for nitroaromatic explosives detection. *J. Mater. Chem.* **2006**, *16*, 2871–2883.

(23) McQuade, D. T.; Pullen, A. E.; Swager, T. M. Conjugated Polymer-Based Chemical Sensors. *Chem. Rev.* **2000**, *100*, 2537–2574.

(24) Eiceman, G. A.; Stone, J. A. Peer Reviewed: Ion Mobility Spectrometers in National Defense New uses of previously unheralded analytical instruments. *Anal. Chem.* **2004**, *76*, 390A–397A.

(25) Sylvia, J. M.; Janni, J. A.; Klein, J. D.; Spencer, K. M. Surface-Enhanced Raman Detection of 2,4-Dinitrotoluene Impurity Vapor as a Marker To Locate Landmines. *Anal. Chem.* **2000**, *72*, 5834–5840.

(26) Furton, K.; Myers, L. J. The scientific foundation and efficacy of the use of canines as chemical detectors for explosives. *Talanta* **2001**, *54*, 487–500.

(27) Håkansson, K.; Coorey, R. V.; Zubarev, R. A.; Talrose, V. L.; Håkansson, P. Low-mass ions observed in plasma desorption mass spectrometry of high explosives. *J. Mass Spectrom.* **2000**, *35*, 337–346.

(28) Hollowell, S. Screening people for illicit substances: a survey of current portal technology. *Talanta* **2001**, *54*, 447–458.

(29) Luggar, R. D.; Farquharson, M. J.; Horrocks, J. A.; Lacey, R. J. Multivariate analysis of statistically poor EDXRD spectra for the detection of concealed explosives. *X Ray Spectrom.* **1998**, *27*, 87–94.

- (30) Sun, X.; Wang, Y.; Lei, Y. Fluorescence based explosive detection: from mechanisms to sensory materials. *Chem. Soc. Rev.* **2015**, *44*, 8019–8061.
- (31) Dong, Y.; Lam, J. W. Y.; Qin, A.; Sun, J.; Liu, J.; Li, Z.; Sun, J.; Sung, H. H. Y.; Williams, I. D.; Kwok, H. S.; Tang, B. Z. Aggregation-induced and crystallization-enhanced emissions of 1,2-diphenyl-3,4-bis(diphenylmethylene)-1-cyclobutene. *Chem. Commun.* **2007**, 3255–3257.
- (32) (a) Wang, L.; Li, W.; Lu, J.; Zhao, Y.-X.; Fan, G.; Zhang, J.-P.; Wang, H. Supramolecular Nano-Aggregates Based on Bis(Pyrene) Derivatives for Lysosome-Targeted Cell Imaging. *J. Phys. Chem. C* **2013**, *117*, 26811–26820. (b) Kasha, M. Energy Transfer Mechanisms and the Molecular Exciton Model for Molecular Aggregates. *Radiat. Res.* **1963**, *20*, 55–71.
- (33) Hong, Y.; Lam, J. W. Y.; Tang, B. Z. Aggregation-induced emission: phenomenon, mechanism and applications. *Chem. Commun.* **2009**, 4332–4353.
- (34) Chen, J.; Law, C. C. W.; Lam, J. W. Y.; Dong, Y.; Lo, S. M. F.; Williams, I. D.; Zhu, D.; Tang, B. Z. Synthesis, Light Emission, Nanoaggregation, and Restricted Intramolecular Rotation of 1,1-Substituted 2,3,4,5-Tetraphenylsiloles. *Chem. Mater.* **2003**, *15*, 1535–1546.
- (35) Tang, B. Z.; Geng, Y.; Lam, J. W. Y.; Li, B.; Jing, X.; Wang, X.; Wang, F.; Pakhomov, A. B.; Zhang, X. X. Processible Nanostructured Materials with Electrical Conductivity and Magnetic Susceptibility: Preparation and Properties of Maghemite/Polyaniline Nanocomposite Films. *Chem. Mater.* **1999**, *11*, 1581–1589.
- (36) Islam, A. S. M.; Sasmal, M.; Maiti, D.; Dutta, A.; Show, B.; Ali, M. Design of a Pyrene Scaffold Multifunctional Material: Real-Time Turn-On Chemosensor for Nitric Oxide, AIEE Behavior, and Detection of TNP Explosive. *ACS Omega* **2018**, *3*, 10306–10316.
- (37) Jiang, L.; Gao, H.; Gai, L.; Shen, Z. J-Aggregation induced emission enhancement of a thienyl substituted bis(difluoroboron)-1,2-bis((1H-pyrrol-2-yl)methylene)hydrazine (BOPHY) dye. *New J. Chem.* **2018**, *42*, 8271–8275.
- (38) Chen, M.; Li, L.; Wu, H.; Pan, L.; Li, S.; He, B.; Zhang, H.; Sun, J. Z.; Qin, A.; Tang, B. Z. Unveiling the Different Emission Behavior of Polytriazoles Constructed from Pyrazine-Based AIE Monomers by Click Polymerization. *ACS Appl. Mater. Interfaces* **2018**, *10*, 12181–12188.
- (39) Kaiser, T. E.; Wang, H.; Stepanenko, V.; Würthner, F. Supramolecular construction of fluorescent J-aggregates based on hydrogen-bonded perylene dyes. *Angew. Chem., Int. Ed.* **2007**, *46*, 5541–5544.
- (40) Dautel, O. J.; Wantz, G.; Almairac, R.; Flot, D.; Hirsch, L.; Lere-Porte, J.-P.; Parneix, J.-P.; Serein-Spirau, F.; Vignau, L.; Moreau, J. J. E. Nanostructuring of Phenylenevinylenediimide-Bridged Silsesquioxane: From Electroluminescent Molecular J-Aggregates to Photoresponsive Polymeric H-Aggregates. *J. Am. Chem. Soc.* **2006**, *128*, 4892–4901.
- (41) Daglar, B.; Demirel, G. B.; Bayindir, M. Fluorescent Paper Strips for Highly Sensitive and Selective Detection of Nitroaromatic Analytes in Water Samples. *ChemistrySelect* **2017**, *2*, 7735–7740.
- (42) Zhang, X.; Hu, J.; Wang, B.; Li, Z.; Xu, S.; Chen, Y.; Ma, X. A chiral zinc(II) metal-organic framework as high selective luminescent sensor for detecting trace nitro explosives picric acid and Fe^{3+} ion. *J. Solid State Chem.* **2019**, *269*, 459–464.
- (43) Che, W.; Li, G.; Liu, X.; Shao, K.; Zhu, D.; Su, Z.; Bryce, M. R. Selective sensing of 2,4,6-trinitrophenol (TNP) in aqueous media with "aggregation-induced emission enhancement" (AIEE)-active iridium(III) complexes. *Chem. Commun.* **2018**, 54, 1730–1733.
- (44) Chakraborty, G.; Mandal, S. K. Design and Development of Fluorescent Sensors with Mixed Aromatic Bicyclic Fused Rings and Pyridyl Groups: Solid Mediated Selective Detection of 2,4,6-Trinitrophenol in Water. *ACS Omega* **2018**, *3*, 3248–3256.
- (45) Pan, J.; Tang, F.; Ding, A.; Kong, L.; Yang, L.; Tao, X.; Tian, Y.; Yang, J. A small-molecule chemosensor for the selective detection of 2,4,6-trinitrophenol (TNP). *RSC Adv.* **2015**, *5*, 191–195.
- (46) Nagendran, S.; Vishnoi, P.; Murugavel, R. Triphenylbenzene Sensor for Selective Detection of Picric Acid. *J. Fluoresc.* **2017**, *27*, 1299–1305.
- (47) Liu, T.; Ding, L.; Zhao, K.; Wang, W.; Fang, Y. Single-layer assembly of pyrene end-capped terthiophene and its sensing performances to nitroaromatic explosives. *J. Mater. Chem.* **2012**, *22*, 1069–1077.
- (48) Kim, S. K.; Lim, J. M.; Pradhan, T.; Jung, H. S.; Lynch, V. M.; Kim, J. S.; Kim, D.; Sessler, J. L. Self-Association and Nitroaromatic-Induced Deaggregation of Pyrene Substituted Pyridine Amides. *J. Am. Chem. Soc.* **2014**, *136*, 495–505.
- (49) Shyamal, M.; Mazumdar, P.; Maity, S.; Sahoo, G. P.; Salgado-Morán, G.; Misra, A. Pyrene Scaffold as Real-Time Fluorescent Turn-on Chemosensor for Selective Detection of Trace-Level Al(III) and Its Aggregation-Induced Emission Enhancement. *J. Phys. Chem. A* **2016**, *120*, 210–220.
- (50) Yue, X.-l.; Wang, Z.-q.; Li, C.-r.; Yang, Z.-y. Naphthalene-derived Al^{3+} -selective fluorescent chemosensor based on PET and ESIPT in aqueous solution. *Tetrahedron Lett.* **2017**, *58*, 4532–4537.
- (51) Liu, B.; Wang, P.-f.; Chai, J.; Hu, X.-q.; Gao, T.; Chao, J.-b.; Chen, T.-g.; Yang, B.-s. Naphthol-based fluorescent sensors for aluminum ion and application to bioimaging. *Spectrochim. Acta, Part A* **2016**, *168*, 98–103.
- (52) Velmurugan, K.; Mathankumar, S.; Santoshkumar, S.; Amudha, S.; Nandhakumar, R. Specific fluorescent sensing of aluminium using naphthalene benzimidazole derivative in aqueous media. *Spectrochim. Acta, Part A* **2015**, *139*, 119–123.
- (53) Tian, J.; Yan, X.; Yang, H.; Tian, F. A novel turn-on Schiff-base fluorescent sensor for aluminum(III) ions in living cells. *RSC Adv.* **2015**, *5*, 107012–107019.
- (54) Saini, A. K.; Sharma, V.; Mathur, P.; Shaikh, M. M. The development of fluorescence turn-on probe for Al(III) sensing and live cell nucleus-nucleoli staining. *Sci. Rep.* **2016**, *6*, 34807.
- (55) Ghorai, A.; Thakur, S. S.; Patra, G. K. The maiden report of a fluorescent-colorimetric sensor for expeditious detection of bifluoride ion in aqueous media. *RSC Adv.* **2016**, *6*, 108717–108725.
- (56) Dutta, K.; Deka, R. C.; Das, D. K. The First Bifluoride Sensor Based on Fluorescent Enhancement. *J. Fluoresc.* **2013**, *23*, 823–828.
- (57) Murugesan, K.; Jeyasingh, V.; Lakshminarayanan, S.; Narayanan, S.; Ramasamy, S.; Enoch, I. V. M. V.; Piramuthu, L. Simple and highly electron deficient Schiff-base host for anions: First turn-on colorimetric bifluoride sensor. *Spectrochim. Acta, Part A* **2019**, *209*, 165–169.
- (58) de Silva, A. P.; Steed, J. W.; Gale, P. A. *Cochrane Clinical Answers*; John Wiley & Sons Ltd, 2012.
- (59) Sahana, A.; Banerjee, A.; Das, S.; Lohar, S.; Karak, D.; Sarkar, B.; Mukhopadhyay, A.; Mukherjee, A. K.; Das, D. A naphthalene-based Al^{3+} selective fluorescent sensor for living cell imaging. *Org. Biomol. Chem.* **2011**, *9*, 5523–5529.
- (60) Tayade, K.; Bondhopadhyay, B.; Basu, A.; Chaitanya, G. K.; Sahoo, S. K.; Singh, N.; Attarde, S.; Kuwar, A. A novel urea-linked dipodal naphthalene-based fluorescent sensor for Hg(II) and its application in live cell imaging. *Talanta* **2014**, *122*, 16–22.
- (61) Joshi, B. P.; Lohani, C. R.; Lee, K. H. A highly sensitive and selective detection of Hg(II) in 100% aqueous solution with fluorescent labeled dimerized Cys residues. *Org. Biomol. Chem.* **2010**, *8*, 3220–6.
- (62) Bhuvanes, N.; Velmurugan, K.; Suresh, S.; Prakash, P.; John, N.; Murugan, S.; Thangadurai, T. D.; Nandhakumar, R. Naphthalene based fluorescent chemosensor for Fe^{2+} -ion detection in microbes and real water samples. *J. Lumin.* **2017**, *188*, 217–222.
- (63) Mondal, S.; Bhanja, A. K.; Ojha, D.; Mondal, T. K.; Chattopadhyay, D.; Sinha, C. Fluorescence sensing and intracellular imaging of Al^{3+} ions by using naphthalene based sulphonamide chemosensor: structure, computation and biological studies. *RSC Adv.* **2015**, *5*, 73626–73638.
- (64) Kaur, N.; Singh, N.; Cairns, D.; Callan, J. F. A Multifunctional Tripodal Fluorescent Probe: "Off-On" Detection of Sodium as well

as Two-Input AND Molecular Logic Behavior. *Org. Lett.* **2009**, *11*, 2229–2232.

(65) Shyamal, M.; Mazumdar, P.; Maity, S.; Samanta, S.; Sahoo, G. P.; Misra, A. Highly Selective Turn-On Fluorogenic Chemosensor for Robust Quantification of Zn(II) Based on Aggregation Induced Emission Enhancement Feature. *ACS Sens.* **2016**, *1*, 739–747.

(66) Wei, T.; Li, H.; Wang, Q.; Yan, G.; Zhu, Y.; Lu, T.; Shi, B.; Lin, Q.; Zhang, Y. A simple Schiff base as “naked eye” and fluorescent “on-off” sensor for detecting cyanide in mixed aqueous solution. *Supramol. Chem.* **2016**, *28*, 314–320.

(67) Samanta, S.; Manna, U.; Ray, T.; Das, G. An aggregation-induced emission (AIE) active probe for multiple targets: a fluorescent sensor for Zn²⁺ and Al³⁺ & a colorimetric sensor for Cu²⁺ and F[−]. *Dalton Trans.* **2015**, *44*, 18902–18910.

(68) Singh, A.; Kaur, S.; Singh, N.; Kaur, N. Fluorometric sensing of Hg²⁺ ions in aqueous medium by nano-aggregates of a tripodal receptor. *Org. Biomol. Chem.* **2014**, *12*, 2302–2309.

(69) Yadav, N.; Singh, A. K. Dual anion colorimetric and fluorometric sensing of arsenite and cyanide ions. *RSC Adv.* **2016**, *6*, 100136–100144.

(70) Purkait, R.; Patra, C.; Mahapatra, A. D.; Chattopadhyay, D.; Sinha, C. A visible light excitable chromone appended hydrazide chemosensor for sequential sensing of Al³⁺ and F[−] in aqueous medium and in Vero cells. *Sens. Actuators, B* **2018**, *257*, 545–552.

(71) Farrugia, L. J. ORTEP-3 for Windows—a version of ORTEP-III with a Graphical User Interface (GUI). *J. Appl. Crystallogr.* **1997**, *30*, 565–565.

(72) Sheldrick, G. M. A short history of SHELX. *Acta Crystallogr., Sect. A: Found. Crystallogr.* **2008**, *64*, 112–122.

(73) Spek, A. L. *Platon: The Netherlands*, 1999.

(74) Frisch, M. J.; Trucks, G. W.; Schlegel, H. B.; Scuseria, G. E.; Robb, M. A.; Cheeseman, J. R.; Scalmani, G.; Barone, V.; Mennucci, B.; Petersson, G. A.; Nakatsuji, H.; Caricato, M.; Li, X.; Hratchian, H. P.; Izmaylov, A. F.; Bloino, J.; Zheng, G.; Sonnenberg, J. L.; Hada, M.; Ehara, M.; Toyota, K.; Fukuda, R.; Hasegawa, J.; Ishida, M.; Nakajima, T.; Honda, Y.; Kitao, O.; Nakai, H.; Vreven, T.; Montgomery, J. A., Jr.; Peralta, J. E.; Ogliaro, F.; Bearpark, M.; Heyd, J. J.; Brothers, E.; Kudin, K. N.; Staroverov, V. N.; Kobayashi, R.; Normand, J.; Raghavachari, K.; Rendell, A.; Burant, J. C.; Iyengar, S. S.; Tomasi, J.; Cossi, M.; Rega, N.; Millam, J. M.; Klene, M.; Knox, J. E.; Cross, J. B.; Bakken, V.; Adamo, C.; Jaramillo, J.; Gomperts, R.; Stratmann, R. E.; Yazyev, O.; Austin, A. J.; Cammi, R.; Pomelli, C.; Ochterski, J. W.; Martin, R. L.; Morokuma, K.; Zakrzewski, V. G.; Voth, G. A.; Salvador, P.; Dannenberg, J. J.; Dapprich, S.; Daniels, A. D.; Farkas, O.; Foresman, J. B.; Ortiz, J. V.; Cioslowski, J.; Fox, D. J. *Gaussian 09*, Revision D.01; Gaussian Inc: Wallingford, CT, 2009.

(75) Becke, A. D. Density-functional thermochemistry. III. The role of exact exchange. *J. Chem. Phys.* **1993**, *98*, 5648–5652.

(76) Cossi, M.; Barone, V. Time-dependent density functional theory for molecules in liquid solutions. *J. Chem. Phys.* **2001**, *115*, 4708–4717.

(77) Cossi, M.; Rega, N.; Scalmani, G.; Barone, V. Energies, structures, and electronic properties of molecules in solution with the C-PCM solvation model. *J. Comput. Chem.* **2003**, *24*, 669–681.

(78) O’Boyle, N. M.; Tenderholt, A. L.; Langner, K. M. cclib: a library for package-independent computational chemistry algorithms. *J. Comput. Chem.* **2008**, *29*, 839–845.